Ph.D. DISSERTATION

Chemoresistive gas sensing properties of functionalized two-dimensional materials

By

Seo Yun Park

February 2020

SEOUL NATIONAL UNIVERSITY

COLLEGE OF ENGINEERING

DEPARTMENT OF MATERIALS SCIENCE AND ENGINEERING

Chemoresistive gas sensing properties of functionalized two-dimensional materials

Advisor: Prof. Ho Won Jang

by

Seo Yun Park

A thesis submitted to the Graduate Faculty of Seoul National University in partial fulfillment of the requirements for the Degree of Doctor of Philosophy

Department of Materials Science and Engineering

December 2019

Approved

By

Chairman of Advisory Committee: Gwan-Hyoung Lee

Vice-Chairman of Advisory Committee: Ho Won Jang

Advisory Committee: Jong-Heun Lee

Advisory Committee: Soo Young Kim

Advisory Committee: Jeong-Yun Sun

Abstract

With the development of the Internet of things (IoT) technology that enables information exchange with all users and devices connected to things, smart sensors that exchange information inside and outside the device are becoming the most important technologies. In particular, the gas sensor is of great interest because it can detect the presence and concentration of a gas and can be applied to a number of areas such as human life, safety, health, and environment monitoring. To be applied to the Internet of Things or next-generation devices, gas sensors must meet all the demanding requirements of low power consumption, low cost, miniaturization, and easy integration with existing technologies. To date, semiconducting metal oxides have been used most often as gas sensing materials due to several advantages such as mass production, miniaturization, low cost, and high gas reactivity at high temperatures. However, there is still a lot of efforts in search of alternative gas sensing materials without solving the main problems such as high-power consumption, use of external heater, weak long-term stability, low humidity durability, and the requirements of the Internet of Things.

Among the materials proposed as alternatives, two-dimensional (2D) materials such as graphene, transition metal dichalcogenide, and metal oxide nanosheets are receiving great attention. 2D materials are evaluated for their ability to replace metal oxides and be applied to future technologies because of their unique and superior advantages, such as flexibility, high specific surface area, many active sites and good room temperature gas sensing properties. It is attracting attention as the next generation gas sensing material because it can improve and solve the disadvantages of the unique properties of 2D materials through

surface functionalization, noble metal decoration, and understanding of the sensing mechanism, and maximize the advantages. In addition, it satisfies the requirements of actual equipment application such as low temperature gas detection, low cost, mass production and miniaturization, and easy to apply to existing technology. However, two-dimensional materials also have disadvantages that must be overcome, such as low selectivity, long response and recovery times, and irreversible gas detection properties.

Therefore, this paper is based on a reduced graphene oxide (rGO)/Molybdenum disulfides (MoS_2) hybrid composite-based humidity sensor manufactured using 1) chemical fabrication such as hydrothermal methods and 2) mechanical fabrication method. Finally, 3) noble metal decorated MoS_2 based gas sensor array are introduced. The detection characteristics of a resistive gas sensor are presented, which solves the problem of power consumption, and low selectivity.

First of all, rGO/MoS_2 composites were synthesized by a simple hydrothermal synthesis method. The gas-sensing properties were confirmed by drop-casting the synthesized material on the interdigitated electrodes manufactured through the photolithography process. Sensors based on the rGO/MoS_2 composites showed high sensitivity, selectivity, and reversible sensing response to relative humidity (RH) at room temperature. The theoretical detection limit was calculated to be about 0.01783% RH level. This sensor not only shows stable operation even in a curved form, but also expands the potential for practical application to next-generation technologies such as the Internet of Things and wearable electronics based on an easy manufacturing process.

Secondly, the room temperature and humidity sensing characteristics of the rGO/MoS_2 van der Waals composites were confirmed by a simple solution process. Sensors based on

the rGO/MoS_2 van der Waals composites showed improved response, selectivity, and reversibility to RH over other gases, and the computational room temperature detection limit was very sensitive, 0.0109% RH. This sensor not only shows stable operation even in a bent flexible device but has also been proven to operate as it is after a long period of more than a year. The excellent humidity sensing characteristics, long-term stability and flexible device applications extend the applicability of the actual gas sensor to the rGO/MoS_2 van der Waals composites.

Thirdly, the noble metal was decorated on the surface of the MoS_2 prepared by using a solution process, and the gas sensing properties were measured. In this study, Pd, Au, and Pt were synthesized on the surface of MoS_2, and compared to the case of using pristine MoS_2, the selectivity was improved. Based on a very simple manufacturing process and excellent gas sensing characteristics, it is possible to confirm the potential of two-dimensional MoS_2 as the next generation gas sensing material.

Keywords: chemoresistive gas sensor, MoS_2, two-dimensional materials, functionalization, gas sensor array

Student Number: 2015-20816

Seo Yun Park

Table of Contents

List of Figures

Chapter 1.

Chemoresistive gas sensing of two-dimensional materials: Principles and leading materials

1.1. Introduction

The olfactory sense is one of the five primary senses (vision, hearing, smell, taste, and touch) of human beings. Predominantly, taste and smell are used to detect flavor. However, the olfactory sense is a major factor in detecting and distinguishing the flavors of different products. In addition, there are typically hundreds of indoor chemicals in the atmosphere, including combustion by-products nitrogen dioxide (NO_2), sulfur dioxide (SO_2), carbon monoxide (CO), and several volatile organic compounds (VOCs). Despite very low concentrations, some of these compounds are very toxic, such as NO_2 and CO. Therefore, monitoring air quality is crucial to maintaining the safety and health conditions. Artificial olfaction is a biomimetic olfactory system[1], which can protect the experts who are required to work in hazardous air environments or improve the quality of life by diagnosing diseases and controlling air quality in daily life. Recently, artificial olfaction has been developed for numerous industry applications[2], such as indoor air-quality monitoring[3], medical care[2,4,5], customs security[6], food quality control[7–13], environmental quality monitoring[14–16], military applications[17], and hazardous gas detection[18,19].

Gas sensor is a technological device that transforms chemical information, originated from a chemical reaction of the analyte of from a physical property of the system, into an analytically useful signal[20]. Gas sensors can be classified

according to the operating principle as shown in Table 1.1. Among them, resistive semiconductor gas sensors receive the most attention owing to their several advantages such as low cost, high sensitivity, simple construction, and high compatibility with microelectronic processing. The most common sensing materials are metal oxide semiconductors (MOS)[21–24]. MOS have been extensively used over the past decades for chemoresistive gas sensor due to their advantages of low cost, small size, and high sensitivity to gas molecules[25–27]. However, metal oxides have major drawbacks that it is very influenced by surrounding environment during measurement and low selectivity, brittleness which hinder the use of metal oxides in next-generation technologies such as wearable devices and electronic nose.

Recently, two-dimensional (2D) materials such as graphene, metal oxide nanosheets, and transition metal dichalcogenides are gaining increasing attention as prospective sensing materials due to high surface-to-volume ratios, and surface configurations including dangling bonds on the edge sites and basal planes can be easily modified by decoration and functionalization process[28,29]. Moreover, unique properties such as flexibility, high transparency, and easy fabrication process are suitable for high performance gas sensors[30,31].

In this thesis, chemoresistive gas sensing properties of 2D materials such as graphene oxide and MoS_2 are presented, also the improvement of sensing

properties of the 2D materials using functionalization and noble metal decorations are investigated. The thesis not only reports sensing performances of the sensors, but also demonstrates sensing mechanism depending on surface configurations, synthetic methods, and surface functional groups on surfaces. The observations on chemoresistive sensing properties of various 2D materials with different device designs and the investigations on sensing mechanisms will broaden the potential and lay the groundwork for 2D materials to be applied in practical applications such as wearable devices and electronic nose.

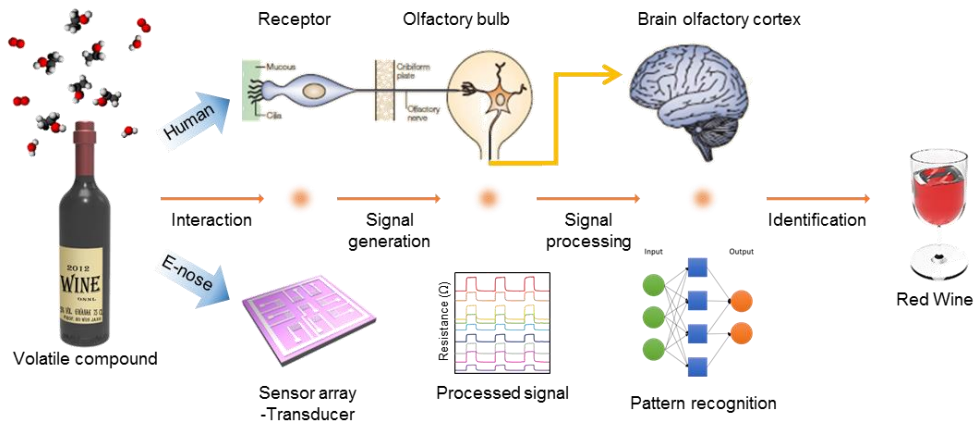

Figure 1.1. Comparison of the mammalian olfactory system and the e-nose system[32]

Table 1.1. Characteristics of diverse types of gas sensors.

Type of gas sensor	**Advantage**	**Disadvantage**
Optical	High sensitivity, selectivity and stability, long Lifetime, Insensitive to environment change	Difficulty in miniaturization, high cost
Electrochemical	High sensitivity, Low power requirements and good resolution, Does not get poisoned by other gas	Limited temperature range, Short of limited shelf life
Catalytic	Small size, Inexpensive operating costs	Highly sensitive to environment change, Baseline drift, Low sensitivity to NH_3 and CO_2
Semiconductor	Low cost, Short response time, Wide range of target gases	Relatively low sensitivity and selectivity, Sensitive to environmental factors

1.2. Basics of chemoresistive gas sensors

1.2.1. Principles of gas sensing mechanisms

Semiconductor gas sensors operate by detecting changes in conductivity resulting from gas adsorption and desorption. In general, changes in the electrical properties of a sensor caused by the adsorption of gas molecules are mainly related to oxygen chemisorption.[21,33] Molecular oxygen adsorbs on the surface of oxide materials by attracting an electron from the conduction band of the semiconductor as shown in the Equation (1).

$$O_2(gas) + e^- \Leftrightarrow O_2^-(adsorb) \quad (1)$$

At high temperature (100 – 400 ℃), the oxygen ion molecules are dissociated into oxygen ion atoms with singly (O^-) or doubly (O_2^-) negative electric charges by trapping an electron again from the conduction band.

$$\frac{1}{2}O_2 + e^- \Leftrightarrow O_{ads}^- \quad (2)$$

$$\frac{1}{2}O_2 + 2e^- \Leftrightarrow O_{ads}^{2-} \quad (3)$$

The oxygen ions on the surface of oxide materials are very active, so undergoing chemical reaction with target gas molecule as shown in the Equation (4)

$$X + O_{ads}^{b-} \rightarrow X' + be^- \quad (4)$$

where X and X' is target gas molecule and out gas after chemical reaction, respectively. The b means the number of electrons.[34]

Based on charge carriers, semiconducting oxide materials can be classified into two groups: *n*-type and *p*-type materials. Target gas species can also be divided into two groups: oxidizing gas (electron acceptors) and reducing gas (electron donor). The chemical reaction causes change of the electric carrier concentration of oxide materials and thus change of gas sensor resistance. The change of gas sensor resistance depends on a type of oxide materials and target gas.

n-type semiconductor gas sensor

Since majority carriers in *n*-type semiconductors are electrons, the electrons in the conduction band of *n*-type semiconductors are removed by the adsorbed oxygen ions. This change in charge carrier concentration causes an increase of resistance of *n*-type semiconductor sensor at operating temperature. When the *n*-type semiconductor sensor is under reducing gas ambient, then a decrease in resistance of the sensor occurs. Conversely, an oxidizing gas cause depletion of charge carrying electrons, resulting in an increase in resistance.

p-type semiconductor gas sensor

A *p*-type semiconductor is one where the majority charge carriers are positive holes. When the oxygen ions are adsorbed on the surface, *p*-type semiconductor generates holes via the excited electrons from valence band resulting in decreasing the sensor resistance (opposite to *n*-type). The opposite effect of *n*-type is also observed showing an increase in resistance in the presence of reducing gas and a decrease in resistance in the presence of oxidizing gas (Figure 1.2).

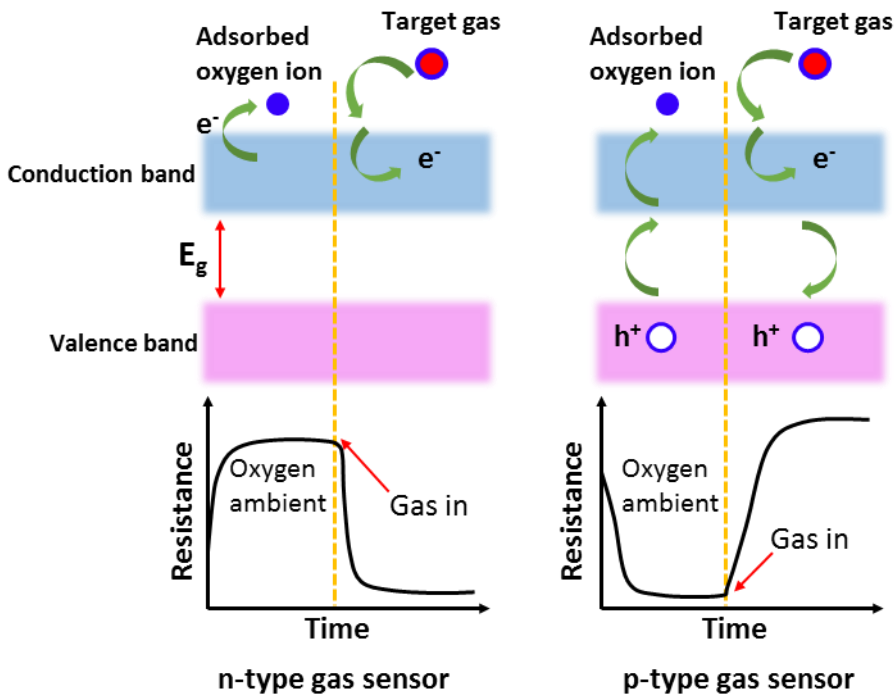

Figure 1.2 Schematic diagram for change of the sensor resistance upon exposure to reducing gas (target gas) in the cases of *n*-type and *p*-type semiconductor sensors.

1.2.2 Gas sensor parameters

Several parameters are used to characterize the performance of the sensor. The most important and essential parameters of the gas sensor and their definitions are listed below.

Response and Sensitivity

Response of semiconductor gas sensors is defined as the ratio of the resistance before and after sensing performance as shown the Equation (5);

$$Response = \frac{R_g}{R_a} \quad \text{or} \quad Response = \frac{R_a}{R_g} \tag{5.1}$$

$$Response\ (\%) = \frac{\Delta R}{R_g} \times 100\ (\%) \tag{5.2}$$

where R_a is the sensor resistance in ambient air, R_g is the sensor resistance in the target gas, and $\Delta R = |R_a - R_g|$.

Sensitivity (S) of gas sensor is a change of measured signal (i.e. response) per analyte concentration; it can be represented by slope of a calibration graph. This parameter is sometimes confused with the limit of detection.

Response and recovery time

Response time is the time it takes for sensor to undergo resistance changing from 10% to 90% of the value in equilibrium upon exposure to target gas. Recovery time is the time required for the sensor signal to return to 90% of its initial value upon removal of the target gas (Figure 1.3).

Limit of detection

Limit of detection is defined as the lowest concentration of the target gas that can be detected by the gas sensor under given conditions. Limit of detection is estimated via extrapolating of sensitivity versus concentration curve and using the following equation. (6)

$$Limit\ of\ detection = \frac{3.3 \times \sigma}{Slope\ (s)} \quad (6)$$

where σ is standard deviation of the regression line (Figure 1.4).[35]

Selectivity

Selectivity represents characteristics that determine whether a gas sensor can respond selectively to a specific analyte or a group of analytes.

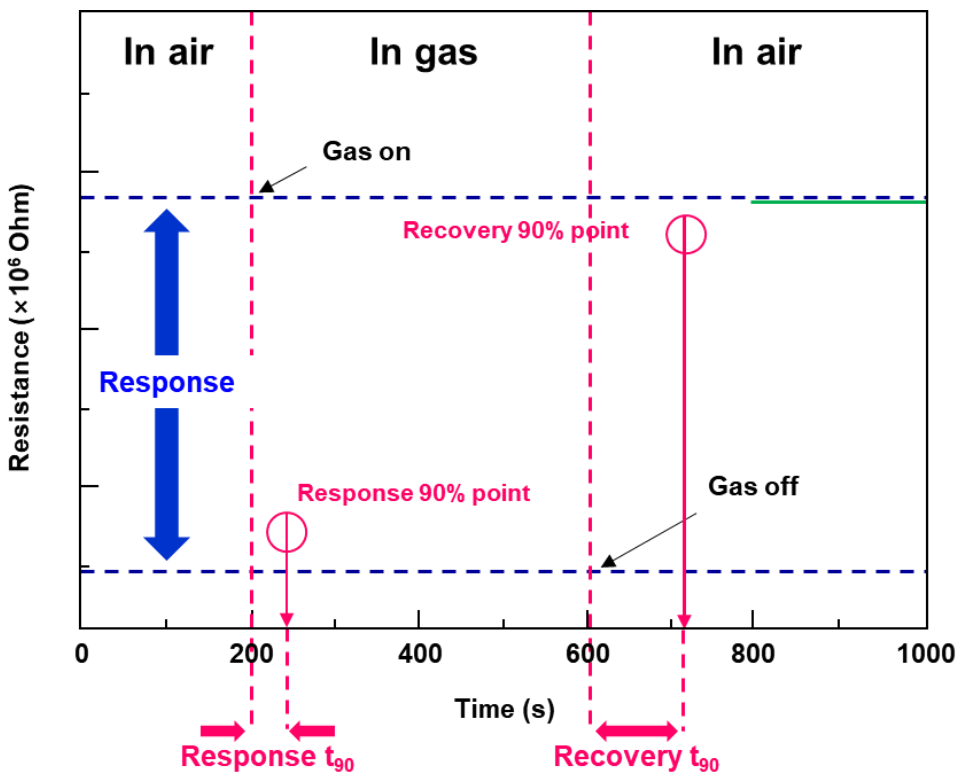

Figure 1.3. Definition of response and recovery time.

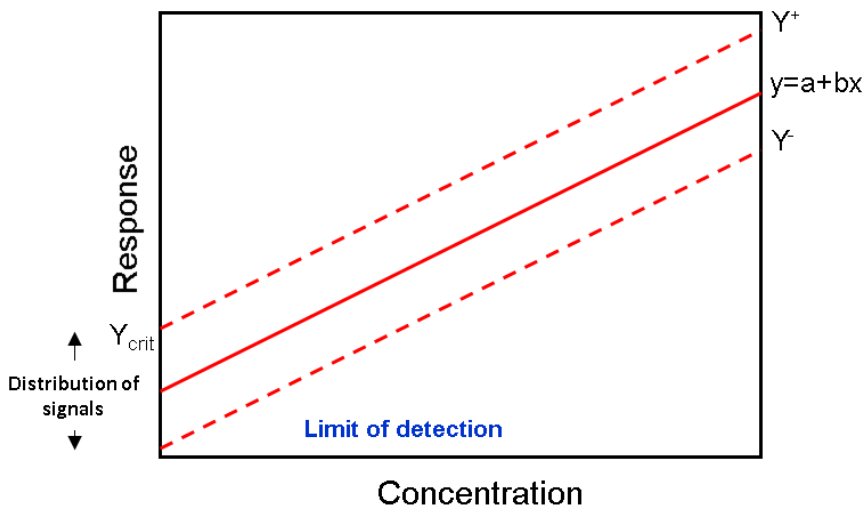

Figure 1.4. Limit of detection estimation. Extrapolating line (y=ax+b) and graphical deduction of limit of detection. The arrow on the y axis reflects the maximum future signal (responses) height.[35]

1.2.3. Three basic factors for chemoresistive gas sensing

The gas sensing properties of chemoresistive gas sensors are affected by three basic factors: receptor function, utility factor, and transducer function. Figure 1.5 shows the schematic diagram for concept of three basic factors. The receptor function refers to how the surface of sensing materials interact with gas molecules. It is possible to enhance sensing responses by modification of surface chemistry. In particular, surfaces of 2D materials with numerous active edge sites and defects can be easily modified by simple functionalization and surface decoration processes that enhance gas selectivity. Since the nanoscale noble metals have catalytic effect for preferred selective detection of specific gas species, they effectively enhance the receptor function. Utility factor is the ability of inner sites of sensing materials to access the target gas which have relevance to porosity of sensing layers and diffusion depth of gas molecules. For instance, the sensing ability can be lower when the sensing layer is too thick and the pore size is too small at the same time because gas molecules cannot pass through the sensing body. Transducer function expresses the ability to convert the signal generated by gas adsorption into an electrical signal like current, and resistances. Shape and configuration of sensing layers can tune transducer function. Hence, in order to achieve high gas sensing performance, the three basic factors should be properly controlled.

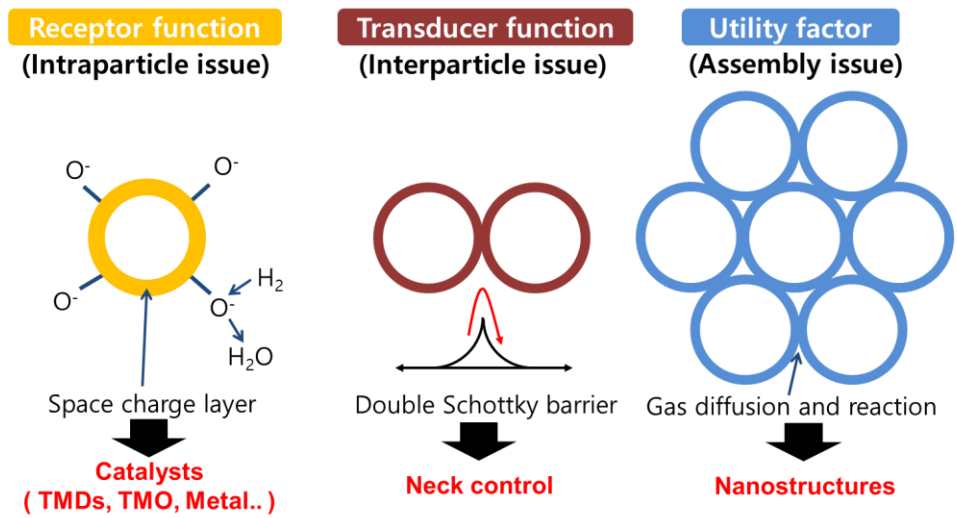

Figure 1.5. Schematic diagram of three basic factors in chemoresistive gas sensing

1.3. Two-dimensional materials for chemoresistive gas sensing

1.3.1. Graphene-based gas sensors

Graphene composed of a single layer of carbon honeycomb lattice is considered as a promising material for next generation of high-performance sensing application, because all atoms of the graphene are surface atoms, the electrical noise level is very low, and characteristics can be easily adjusted by a simple procedures. For these reasons, many research groups are investigating chemo-resistive gas sensing applications based on graphene derivatives, such as graphene, graphene oxide, and reduced graphene oxide.

Shedin *et al*.[36] reported capability of detecting individual gas molecules using microscale graphene gas sensor (Figure 1.6). In the report, Shedin *et al*. found that the initial undoped state could be recovered by annealing at 150 °C in vacuum (region IV in Figure 1.6). Repetitive exposure–annealing cycles showed no 'poisoning' effects of these chemicals (that is, the devices could be annealed back to their initial state). Lipatov *et al*.[37] reported reduced graphene oxide (rGO) gas sensor based gas sensor array addressing the selectivity problem. With irregular structure of rGO films at different levels of organization, ranging from nanoscale to microscale, the rGO based sensor array demonstrated a high selectivity that can classify different alcohols, such as methanol, ethanol and isopropanol (Figure 1.7). Pour *et al*.[38] reported the development of graphene nanoribbon based sensor array

using solution process on the KAMINA platform. Pour *et al.* found that the lateral extension of graphene nanoribbons resulted in a reduction in the electronic bandgap, improving the conductivity of the graphene and enhancing the response to low molecular weight alcohols (Figure 1.8.). Dan *et al.*[39] demonstrated that the contamination layer chemically dopes the graphene, enhanced carrier scattering, and acted as an absorbent layer that concentrates analyte molecules at the graphene surface, thereby enhancing the sensor response.

On top of this, there is a lot of researches on chemoresistive gas sensors based on graphene derivatives.[40–43] This research attempts to provide high-performance gas sensors with high sensitivity, reversibility, and selectivity, but remains an open question. Delays in response and recovery, high power consumption, sophisticated structures, and the flexibility of the device have hindered the practical application of the sensor. Therefore, I report a variety of approaches, such as functionalization and surface decoration to enhance the selectivity of MoS_2 based materials.

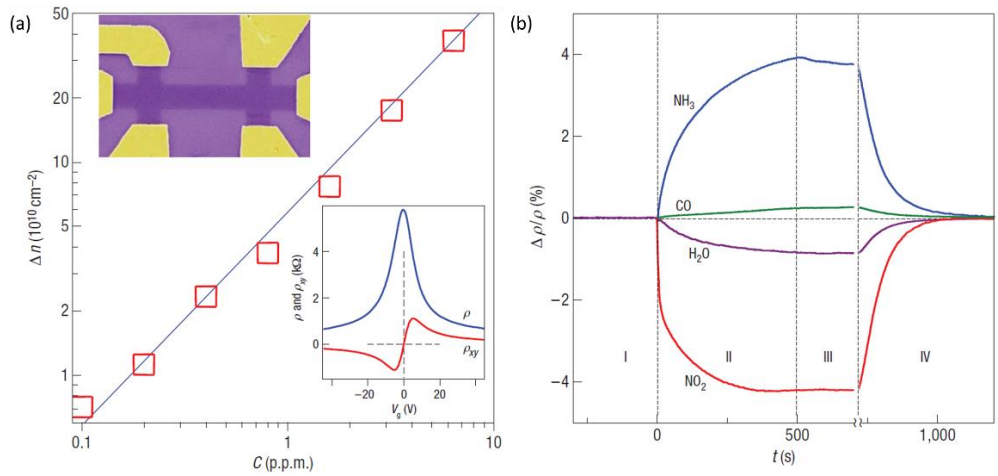

Figure 1.6. Sensitivity of graphene to chemical doping. (a) Concentration of chemically induced charge carriers in single-layer graphene exposed to different concentrations of NO_2. Upper inset: SEM. Lower inset: Characterization of the graphene device by using the electric-field effect. (b) Changes in resistivity upon exposure to various gases of 1 ppm.[36]

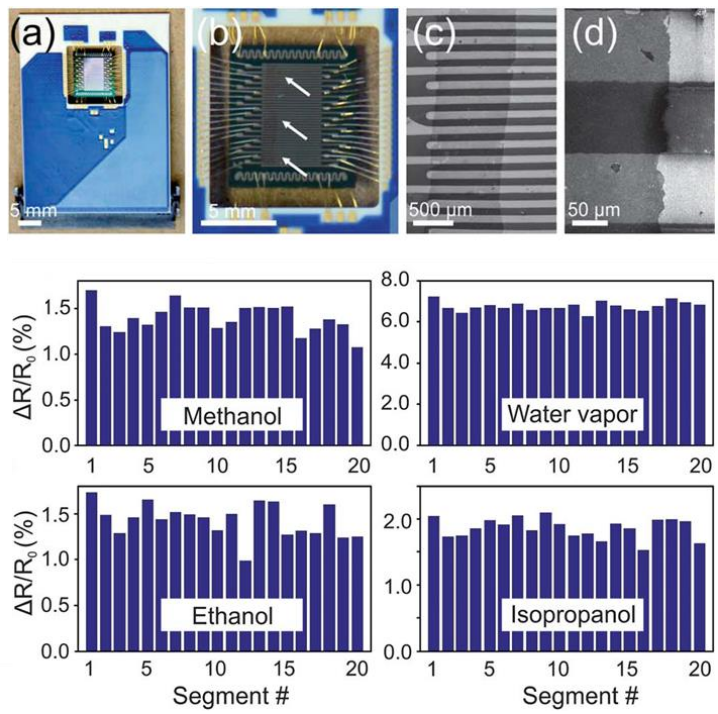

Figure 1.7. (a) Optical image of a KAMINA platform based on reduced graphene oxide and (b) active area of the sensor. (c) SEM image of sensors deposited with rGO and (d) a fragment of one of the devices shown in (c). (e) Distributions of gas responses of rGO segments to 1500 ppm of methanol, water vapor, ethanol and isopropanol mixed with dry air.[37]

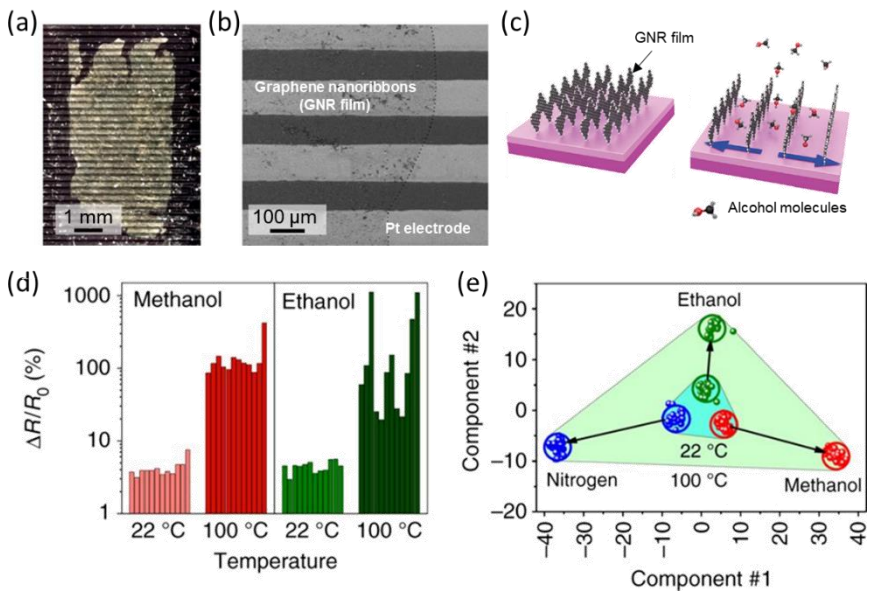

Figure 1.8. (a) Optical image of KAMINA chip with a GNR film deposited on the multielectrode. (b) SEM image of the random GNR film segments on the multielectrode structure. The edge of the GNR film is shown by the dotted curve. (c) Schematic image of GNR film on the substrate and the possible intercalation of alcohol molecules which might induce the decrease in the conductivity of the eGNR film. (d) Representative dynamic responses at room temperature and 100 °C to 500 ppm methanol and ethanol with selected fragment of the GNR sensor array. (e) The results of LDA processing of the responses obtained by GNR sensor array exposed to nitrogen mixed with 500 ppm of ethanol and methanol at 22 °C (small blue triangle) and 100 °C (large green triangle).[38]

1.3.2. Transition metal dichalcogenides based gas sensors

Due to the increasing interest in two-dimensional materials, transition metal dichalcogenides (TMDs) such as MoS_2, WS_2, SnS_2, WSe_2, and $NbSe_2$ are being studied as gas sensing materials.[44–51] In contrast to graphene-based materials, TMDs have other advantages, such as semiconducting nature, and numerous active edge sites.

Ou *et al.*[44] demonstrated reversible and selective sensing properties of 2D SnS_2 flakes to NO_2 exposures at low operating temperatures of less than 160 °C (Figure 1.9). The optimal sensing temperature was 120 °C showing excellent linearity with increasing NO_2 concentration from 0.6 to 1.2 ppm. Ko *et al.*[45] reported Ag nanowire decorated large-area 2D WS_2 based NO_2 gas sensor with high response and significantly improved recovery. Late *et al.*[46] reported gas sensing behavior of few MoS_2 layers using transistor geometry. The sensor exhibited excellent sensitivity, and recovery. The sensing mechanism was investigated by DFT calculations (Figure 1.10). Cho *et al.*[50] presented chemoresistive gas sensing properties of 2D $NbSe_2/WSe_2$ layered junction which is applicable on wearable devices. They showed high endurance to mechanical bending and doing laundry as well.

As noted above, many researchers have explored TMDs based chemoresistive gas sensors to demonstrate impressive chemoresistive sensing properties such as high

selectivity, sensitivity, and reversibility compared to other 2D materials. Despite the great potential for high performance gas sensors, selectivity and recovery problem still remains. Therefore, this paper uses several methods to improve selectivity and recovery of TMDs based gas sensors.

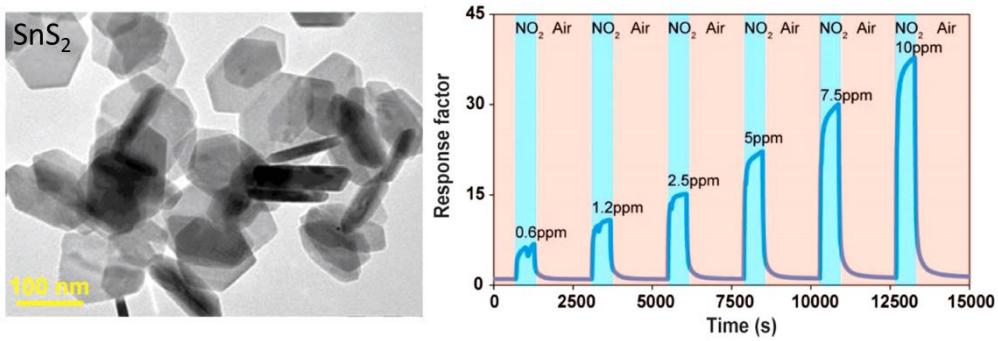

Figure 1.9. TEM image of 2D SnS_2 and the sensing responses to NO_2 gas operated at 120 ^oC.[44]

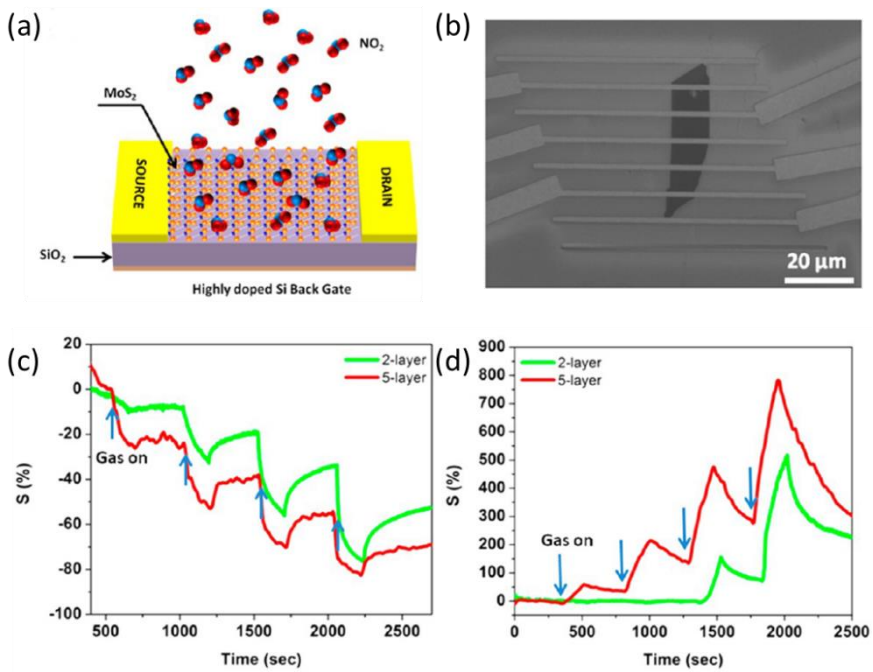

Figure 1.10. (a) Schematic of the MoS_2 transistor-based NO_2 gas-sensing device. (b) SEM image of two-layer MoS_2 transistor device. Sensing curves to (c) NH_3 and (d) NO_2.[46]

Chapter 2

Room temperature humidity sensors based on rGO/MoS_2 hybrid composites synthesized by hydrothermal method

2.1. Introduction

The growth of Internet of things (IoT), interconnection between objects which possess the technology that detect and propagate internal and external state of the object, have opened new opportunities for gas sensors [52]. In previous study, low or high level of relative humidity can induce some physical discomfort such as respiratory or skin problems [53]. Controlling and monitoring humidity have gained great interest in IoT including building automation, agriculture, aerospace, semiconductor industry and healthcare [54–56]. For the IoT, however, the device should satisfy special requirements like high response, selectivity, reliability, low-cost mass production, and low power consumption.

Electronic type humidity sensors are classified into two types by measuring methods: capacitive and resistive-type humidity sensors. Capacitive-type humidity sensors are extensively exploited due to their numerous advantages such as low power consumption, good linearity, and wide range of relative humidity (R.H.) detection. However, complex device structure and expensive price due to complicated fabrication process still remain as challenges to be overcome [57–59]. In the contrast, resistive-type humidity sensors have merits of simple fabrication, cost effectiveness, and small size which can be easily applied to sensor array [56,60–64].

For resistive-type humidity sensors, metal oxide [65] and polymer [66] have been studied, but considerable problems have been remained: Wang *et al.* [21] have

revealed that metal oxide based humidity sensors show significant degradation of the sensor performance under humid ambient. Wang *et al.* [67] also showed polymer based humidity sensors exhibit inherent drawbacks of poor stability in high humidity environment, thus limit their further development. To overcome these problems, other types of materials have been studied as alternative sensing elements.

Two-dimensional (2D) materials, such as graphene and transition metal dichalcogenides (TMD), with large surface to volume ratio, high specific area, and numerous active sites have demonstrated great potential as sensing materials [36,38,68–70]. Reduced graphene oxide (rGO), one of the graphene derivatives, is a very fascinating material for humidity detection [40,71,72] because rGO has oxygen-containing functional groups such as –COOH and –OH on the surface which show hydrophilicity [73,74]. Moreover, rGO can be fabricated by facile and cost-effective processes that can be ready for mass-production [75]. In addition, molybdenum disulfide (MoS_2) is attracting considerable attention as a humidity sensing material due to its remarkable sensing performance originating from numerous dangling bonds at the edge sites [46,48]. Taking both advantages of the materials, rGO/MoS_2 hybrid composites are utilized for humidity sensors [61,76]. Hydrothermal synthesis has the advantage of a liquid phase process that can produce crystalline anhydrous ceramic powder in one process. The main difference from other methods is that

annealing process at high temperature is not required. In other words, not only the annealing process but also the grinding process according to the annealing process is not required. Therefore, it is possible to suppress the inflow of impurities and the occurrence of defects due to grinding. Another advantage of hydrothermal synthesis is that the choice of raw materials to react and the reaction conditions are very wide, not only the use of cheap raw materials, but also the easy control of the physical and chemical properties of the powder. It can satisfy such characteristics as miniaturization of powder size. In addition, the manufacturing process is simple, and a large amount of high purity powder can be obtained from low purity low cost raw materials [77,78].

In the previous research, Novoselov *et al.*, has proven van der Waals bonding formation between 2D materials [79]. When *p*-type rGO [71,80] contacts to intrinsic *n*-type MoS_2 [48], *p*-*n* junction is formed by van der Waals bonding between rGO and MoS_2 [81]. The *p*-*n* heterojunction formed between rGO and MoS_2 interface enhances the humidity sensing performance of rGO and MoS_2 hybrid composites through controlling electronic transport at the hetero-interface and synergistic promotion of humidity sensing reaction[76,81].

Herein, we report extremely sensitive and selective humidity sensors using layered structures of rGO/MoS_2 hybrid composites fabricated by hydrothermal method. Drop-casting methods on Pt electrodes were used to fabricate the sensors

which show a high and linear response to a wide range of RH due to the increased number of active sites and *p-n* junction formation. As taking both advantages of rGO and MoS_2, we present the enhanced sensing properties such as sensitivity, selectivity and response time. The morphology of rGO/MoS_2 hybrid composites was examined by scanning electron microscope (SEM) and transmission electron microscopy (TEM) and the formation of *p-n* junctions are clarified by peak shift of X-ray photoelectron spectroscopy (XPS). Our results here suggest that the fabrication of rGO/MoS_2 hybrid composites through hydrothermal method is an effective method to fabricate highly sensitive and selective humidity sensing materials.

2.2. Experimental section

2.2.1. Synthesis of MS-GO

22 mg of $(NH_4)_2MoS_4$ was added to various concentrations of GO in DMF and stirred at room temperature until the solutions were homogenously mixed. The amount of GO was decided by calculating molar ratio as GO/$(NH_4)_2MoS_4$ to be 5:1, 3:2, 1:5. Next, each solution was well dispersed by using an ultrasonic bath for 20 min, and was then transferred to a 40 mL Teflon-lined autoclave and kept in a convection oven at 200 °C for 10 h. The product was then centrifuged at 8,000 rpm and washed with DI water. Next, the solution was rinsed 5 times to completely remove DMF and organic residues. The final products which consisted of

rGO/MoS_2 hybrid composites (MS-GOs) were re-dispersed in 5 mL DI water. Pristine MoS_2 was prepared by using the same procedure but without the addition of GO. The samples were named each rGO/MoS_2 5:1, 3:2, and 1:5 as MS-GO1, MS-GO2, and MS-GO3.

2.2.2. Sensor fabrication

Electrodes which has 4 µm of interspaces were prepared on a SiO_2/Si substrate using photolithography followed by metal deposition (Pt/Ti) using e-beam evaporator. A 0.4 µL drop of a MS-GO solution was cast onto a Pt finger/SiO_2/Si substrate. To evaporate the DI water, the samples were dried on a hotplate at 100 ^oC for 10 minutes, resulting in sensing materials loading on the substrate.

2.2.3. Material characterization

To ensure successful hybridization of rGO and MoS_2 from GO and $(NH_4)_2MoS_4$ precursors, various characterizations were carried out using SEM, TEM, Raman and XPS. The SEM was performed by using Steroscan 440 (Leica Cambridge) to study the morphology of surface. The high resolution TEM (HRTEM) measurements were accomplished using JEM-2100F (JEOL) performed at an acceleration voltage of 200 kV. The XPS were characterized with K-Alpha (Thermo electron).

2.2.4. Sensor measurements

The humidity sensing properties of rGO, MS-GOs, and MoS_2 based sensor were measured at room temperature by monitoring resistivity change of sensors during switching flow gases from dry air to humid air. The resistance of the sensor was measured under a DC bias voltage of 1 V using a source measurement unit (Keithley 236). The continuous flow rate of 500 sccm was used for both dry and humid air. The response of the sensors was accurately regulated by the ratio of the fully recovered resistances after exposure to humidity to the base resistance in dry air.

2.2.5. Flexible Device

Interdigitated electrodes (IDEs) of 5 μm interspacing were prepared on PET substrate using photolithography followed by metal (Pt/Ti) deposition. The active area for humidity sensing was consist of 20 finger electrodes. 0.5 μl of MS-GO2 was deposited on the Pt/IDEs/PET substrate by drop-casting method, and then dried for 10 min at 100 ^{o}C on a hotplate to remove the solution. To confirm stable sensing operation under bending strain, the flexible device was attached on pen cap (bending radius of 7 mm). The bent sensor was fixed on an alumina plate and loaded to the gas sensing measurement system.

2.3. Result and discussion

2.3.1. Fabrication process and electrical properties

The fabrication process of MS-GO is demonstrated in Figure 2.1. $(NH_4)_2MoS_4$ and graphene oxide in *N,N*-dimethylformamide (DMF) solution was used as precursor material of MS-GO. GO and $(NH_4)_2MoS_4$ were dispersed by ultra-sonication for 10 minutes and then poured in a 40 mL Teflon-lined autoclave. Then MS-GOs were synthesized by hydrothermal method at 200 ^oC for 10 hours. During the fabrication process, $(NH_4)_2MoS_4$ and GO were reduced to MoS_2 and rGO respectively by following equation [82,83] :

$$(NH_4)_2MoS_4 + GO \rightarrow MoS_2 + H_2S + S + NH_3 + rGO.$$

After cooling down to the room temperature, the final product was centrifuged at 8,000 rpm to remove DMF and then washed with DI water. MS-GO was then drop-casted onto a Pt finger electrode with 4-μm interspacing patterned on SiO_2/Si substrate (Figure 2.2a). Both sides of finger electrodes were passivated with insulating material to observe the sensing performance occurred at active area (Figure 2.2b). 0.4 μL of each MS-GOs were drop-casted onto Pt finger electrodes. The MS-GOs were sufficiently distributed on the active area between Pt finger electrodes (Figure 2.2c) and then dried on a hot plate to remove the DI water which can influence on humidity sensing properties. Figure 2.2d, e, and f show SEM images of pristine rGO, MoS_2, and MS-GOs, respectively. From previous study,

MoS_2 was exfoliated by sonication showed the stacked layer structure. However, MoS_2 synthesized by hydrothermal method showed flower-like nanoparticles, composed with nano-sheets. As shown in Figure 2.2f, MoS_2 is well distributed on rGO without noticeable aggregation, resulting in highly exposed edge sites.

TEM images were taken in order to characterize the microstructural information of the samples. Figure 2.3 reveals morphology of pristine MoS_2 (Figure 2.3a, b, and c) and a MS-GO (Figure 2.3d, e, and f). The TEM image of Figure 2.3a indicates the micro-sized MoS_2 particles due to van der Waals stacking of MoS_2, and this is clear in the moire patterns observed in Figure 2.3b due to overlapping of different planes of MoS_2. The interlayer distance of MoS_2 is 0.67 nm matching to the reported MoS_2 (Figure 2.3c). Figure 2.3d shows a MS-GO composite structure with well dispersed layered MoS_2 on rGO bases. From Figure 2.3e, few layered MoS_2 flakes co-exist on rGO are observed, attributing to the selective growth of MoS_2 on oxygen functional groups of GO. (002) basal planes of MoS_2 and interlayer distance of MoS_2 in a MS-GO corresponds with pristine MoS_2 to 0.67 nm (Figure 2.3f). From this TEM image, it is clear that MoS_2 and rGO composites are successfully fabricated.

Figure 2.4a and b display Raman spectra of MS-GO with rGO region (Figure 2.4a) and MoS_2 region (Figure 2.4b). The value of I_D/I_G were 1.20 and 1.14 with rGO, and MS-GO2. The increased intensity ratio of I_D/I_G with rGO and MS-GO2

suggests that GO is successfully reduced to rGO containing some defect sites and created increased number of new sp^2 domains which were presented less in GO. The D peak of GO, rGO, and MS-GO2 are shown in 1347, 1353, and 1357 cm^{-1} respectively and G peak of GO, rGO, and MS-GO2 each are shown in 1591, 1589, and 1607 cm^{-1}. From previous research, D band reveals the structural defects induced from the attachment of oxygen containing functional groups such as hydroxyl and epoxy groups on the basal plane of graphene and its derivatives such as GO and rGO [84]. The G band of the MS-GO2 was shifted to higher frequency confirming the electron interactions between rGO and MoS_2 [85]. And two main peaks shown in Figure 2.4b at 376 and 402 cm^{-1} indicates E^1_{2g} and A_{1g} modes of MoS_2. The intensity of two peaks shows edge terminated characteristics of MoS_2 associated with the lower intensity of E^1_{2g} compared to A_{1g}. Quite a number of unsaturated sulfur atoms exist in the edge site playing an important role in detecting humidity. The chemical properties of MoS_2 are analysed by XPS shown in Figure 2.4c and 4d [84]. In Figure 2.4c, three major peaks at 226, 228.5 and 232 eV correspond to the S 2s of MoS_2, Mo^{4+} $3d_{5/2}$ and Mo^{4+} $3d_{5/2}$ respectively [75,86]. Figure 2.4c shows the absence of MoO_3 because no any other peaks for Mo^{6+} is shown and this can prove that the Mo atoms are not oxidized in MS-GO [87]. The characteristics of sulfur are shown in Figure 2.4d. The peaks shown at 161 and 163 eV correspond to the S $2p_{3/2}$ and S $2p_{1/2}$ of MoS_2. MS-GO2 shows slightly increased binding energy compared to pristine MoS_2 which can be considered as some specific

interaction existing between rGO and MoS_2. The interaction induced by the transfer of electrons between rGO and MoS_2 enhances the conductivity of MS-GOs which can be the evidence of the formation of junction between the interface of rGO and MoS_2. The heterojunctions formed between rGO and MoS_2 are considered to be the reason of increased humidity sensing properties of MS-GOs.

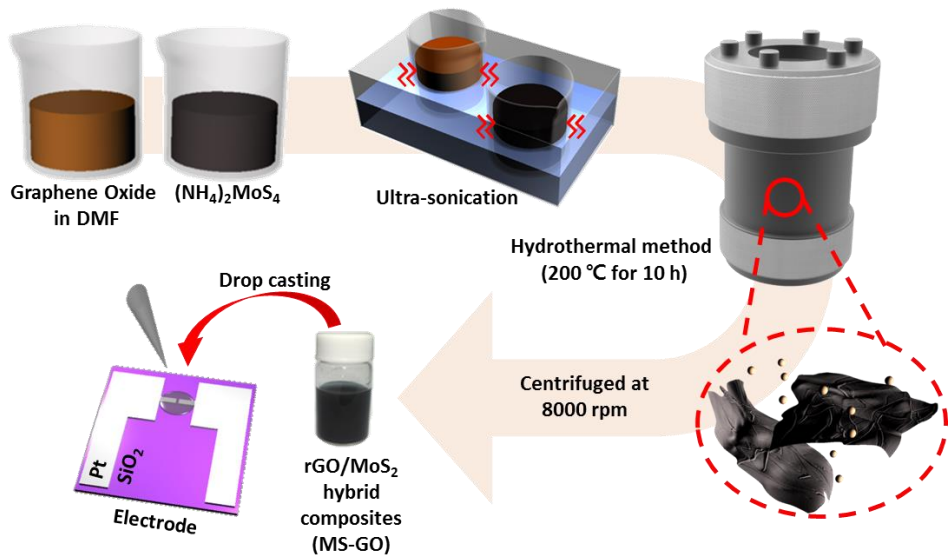

Figure 2.1. Fabrication procedure of MS-GO humidity sensor.

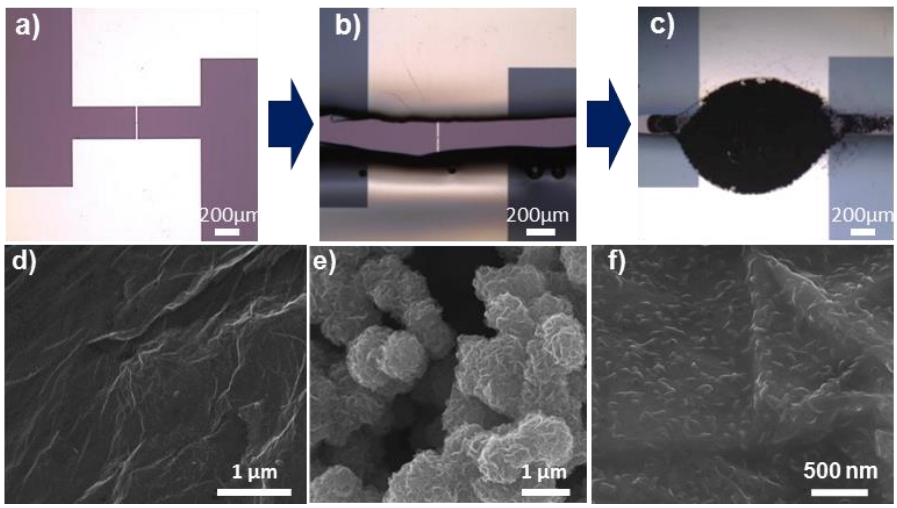

Figure 2.2. (a-c) Optical microscope image of sensing device and the sensing area with MS-GO drop casted. SEM images of (d) rGO, (e) MoS_2 and (f) MS-GO.

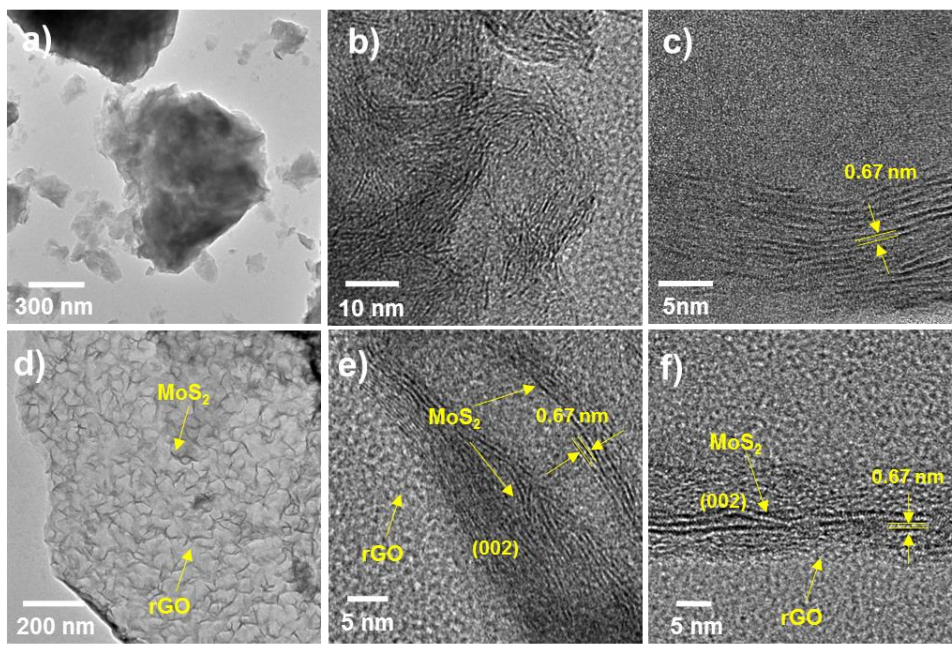

Figure 2.3. TEM images of (a–c) pristine MoS_2 and (d–f) MS-GO

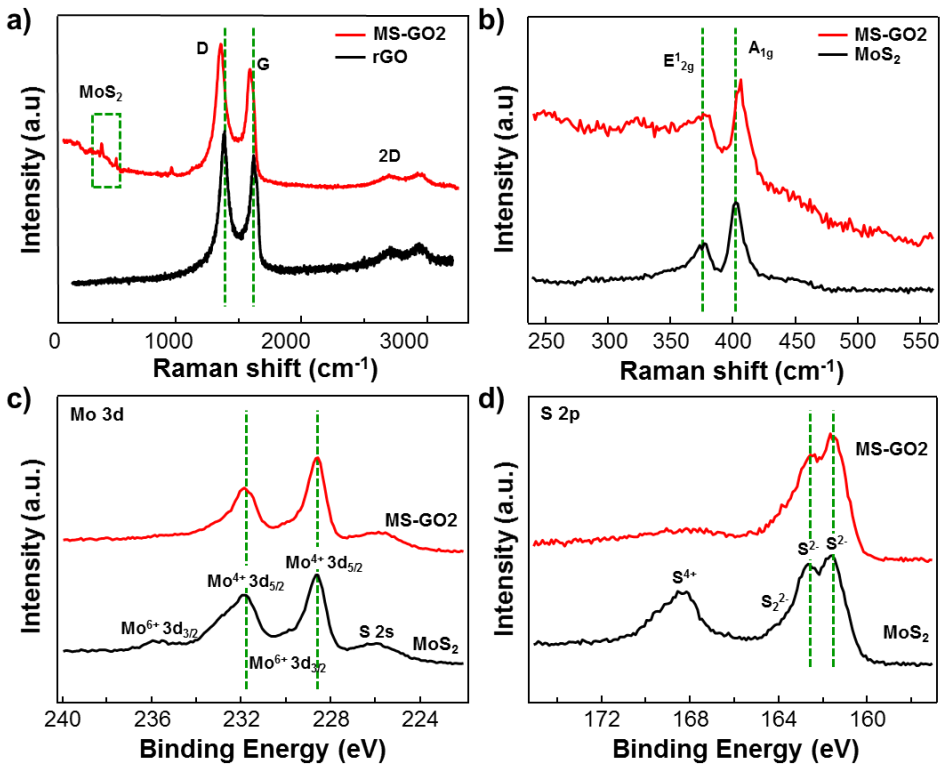

Figure 2.4. Raman spectra of MS-GO hybrids prepared using various GO contents: (a) rGO and (b) MoS_2 peak regions. (c) Mo 3d and (d) S 2p XPS spectra of pristine MoS_2 and of MS-GO with various GO contents.

2.3.2. Gas sensing properties of MS-GO

Figure 2.5 shows the sensing properties of bare rGO, MoS_2 and MS-GO. The dynamic sensing curves of rGO, MS-GO1, MS-GO2, MS-GO3 and MoS_2 are shown in Figure 2.5a. All samples including bare samples possess different base resistances in dry air condition, as shown in the inset data of Figure 2.5b. The bare rGO shows the lowest baseline resistance (5.8×10^3 Ω) and the baseline resistance of pristine MoS_2 is extremely higher up to 1.7×10^8 Ω (Figure 2.6a and e). The samples revealed resistance ranging from 1.0×10^4 Ω to 4.2×10^6 Ω (Figure 2.6b, c, and d). The increase of baseline is in accordance with the increasing concentration of MoS_2. The response to humidity were defined here as $(R_{humidity} - R_{dry})/R_{dry} \times 100$, where R_{dry} and $R_{humidity}$ indicate the resistance of the sensor measured in dry air and in humid air, respectively. The response of rGO, MS-GO1, MS-GO2, MS-GO3 and MoS_2 were calculated to be 3%, 15%, 21%, 14%, and 49% at 50% RH at room temperature (Figure 2.5b). The response time and recovery time for each sample (response t_{90} and recovery t_{90} are the time expended for the resistance to reach 90% of its steady state value in humid response and the recovery to original state, respectively) were calculated (Figure 2.5c). As shown in Figure 2.5c, the response t_{90} of rGO, MSGO1, MS-GO2, MS-GO3 and MoS_2 were 193.7, 59, 30, 116, and 17 s, and the recovery t_{90} of each sample were 418, 343, 253, 282, and 474 s, respectively. While MS-GO2 showed recovery time over 1 minute for

full recovery, humidity sensors based rGO, graphene and MoS_2 sheets exhibited much longer response and recovery time [42,46,88]. Though MoS_2 showed the highest response value but comparing its response and recovery time with other samples, MS-GO2 showed the best sensing performances.

Considering MS-GO2 as the best sample, more detailed sensing properties are measured. MS-GO shows a 4 times higher response than pristine rGO (Figure 2.7a). In order to evaluate the selectivity of MS-GO2 on humidity sensing properties compared to other gases, the responses of MS-GO2 to various gases such as 10 ppm NO_2, 1000 ppm NH_3, 50 ppm H_2, and 50 ppm C_2H_5OH has been measured (Figure 2.8). For comparison, pristine rGO was equally tested. Responses of MS-GO2 to 10 ppm NO_2, 1000 ppm NH_3, 50 ppm H_2, and 50 ppm C_2H_5OH at room temperature are 4, 2.8, 0.2, and 0.3% respectively, while responses of the pristine rGO are 3, 1, 0.1, and 0.4% (Figure 2.7b). From the previous study, pristine rGO and MoS_2 showed good response to NO_2 gas but in this study, MS-GO2 shows extremely high selectivity to humidity [69,85]. This result reveals that the humidity sensing properties of rGO has been significantly enhanced by combining rGO with MoS_2. Since MS-GO2 shows a particularly high response to 50% relative humidity air, suggesting that MS-GO2 is profitable for detect humidity air selectively which is one of the most important factors required for semiconductor gas sensors. Moreover, long reliability is considered as another critical factor for humidity

sensors. In this work, we have confirmed the excellent repeatability of MS-GO1 to humidity without any significant degradation (Figure 2.9).

To evaluate the detection limit of MS-GO2 to humid air, the response of the sensor was measured to 10, 30, 50, 70, and 90% R.H as shown in Figure 2.7c. The $\triangle R/R_o$ values proportionally increase with increasing R.H values. The response values were plotted as a function of the humidity concentration in Figure 2.7d. A simple linear regression fit was plotted to derive the linear correlation between the responses and the concentrations. The linear regression equation is expressed as y = 0.1865x + 7.8615, where y is the response and x is the relative humidity value. The measure of goodness-of-fit of the linear regression, r^2, was calculated to be 0.98. The responses of the sensor are 9.03, 13.91, 17.53, 21.40, and 23.85 to 10, 30, 50, 70, and 90% RH, respectively. Although the H_2O concentration of 1 ppm was the lowest examined experimentally in the present study, the theoretical detection limit was calculated to be approximately 0.01783% R.H [35,85]. This low level of the detection limits to H_2O indicates its possibility of using in various applications such as environmental monitoring, hospital, and laboratory.

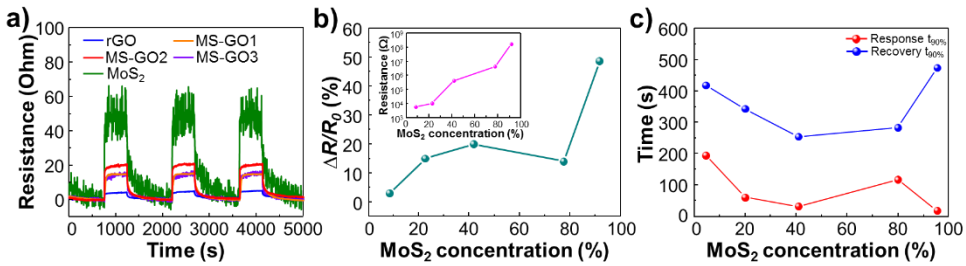

Figure 2.5. (a) Sensing curves of rGO, MS-GO and MoS_2. (b) Responses ($(R_{air} - R_{gas})/R_{gas}$) of rGO and MS-GO to 50% R.H. and resistance of rGO, MS-GO and MoS_2 at 25 ^oC. (c) Response and recovery time at 25 ^oC to 50% R.H.

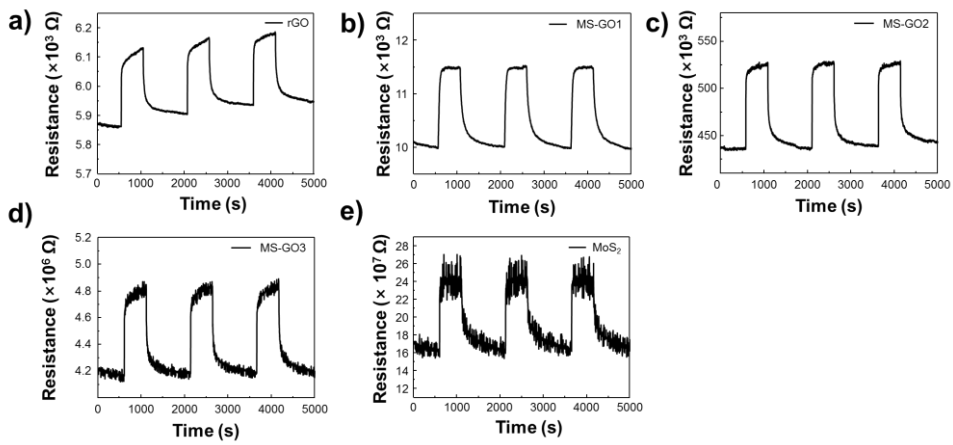

Figure 2.6. Sensing curves of pristine (a) rGO, (b) MS-GO1, (c) MS-GO2, (d) MS-GO3 and (e) MoS_2 to three pulses of 50% R.H

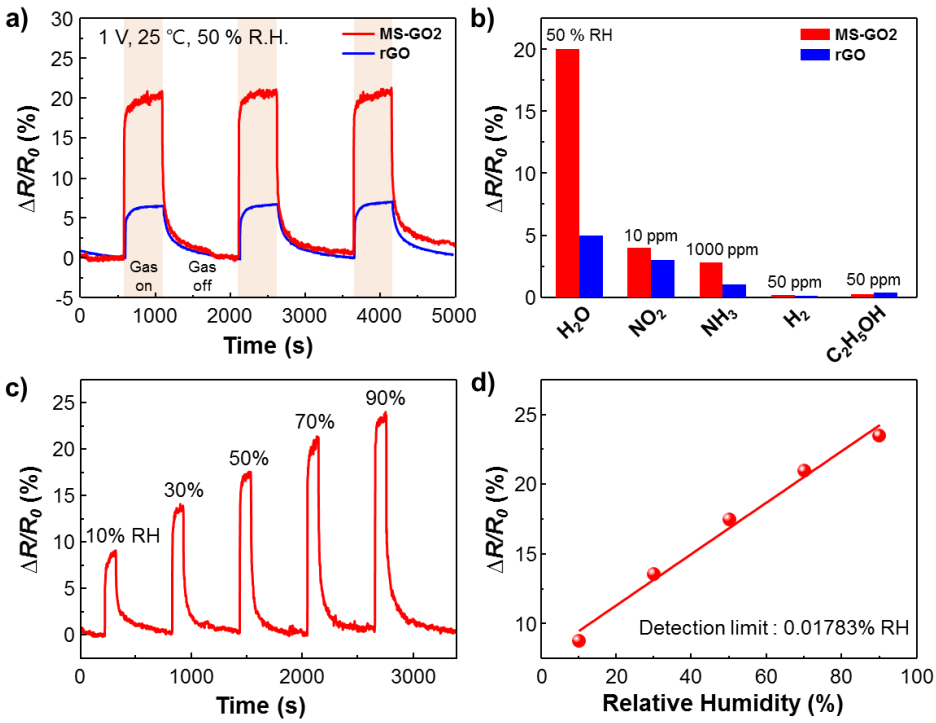

Figure 2.7. Characteristics of the humidity sensors at room temperature. (a) The response curves to (a) 50% R.H. and (b) various types of gases. (c) The response curves and (d) calibration of response toward 10-90 % R.H. at 25°C.

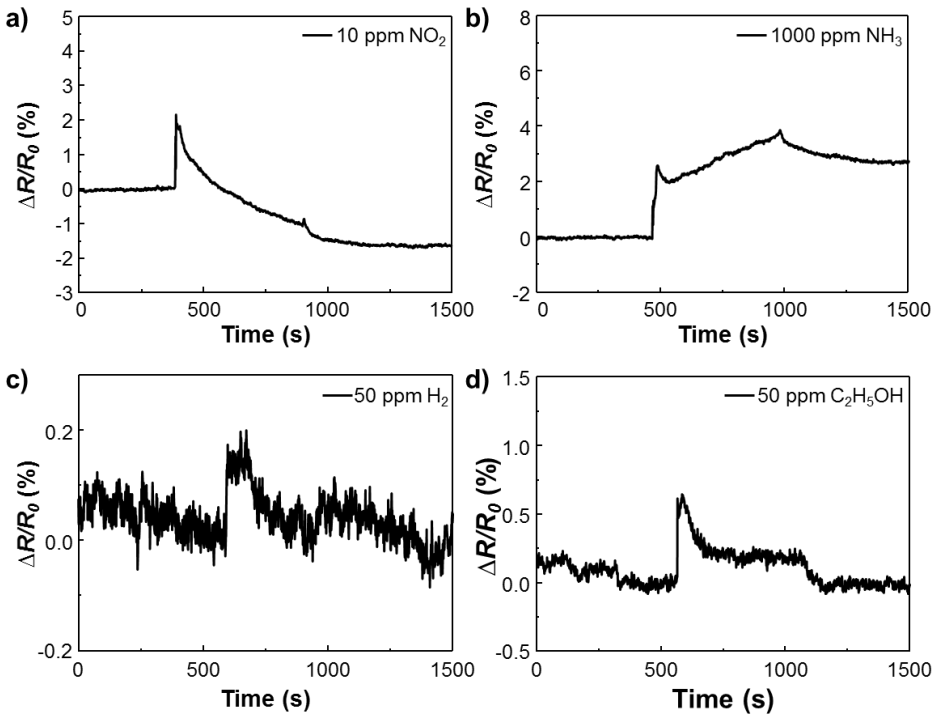

Figure 2.8. Response curves to (a) 10 ppm NO_2 gas, (b) 1000 ppm NH_3 gas, (c) 50 ppm H_2 gas, and (d) 50 ppm C_2H_5OH gas at 25 °C.

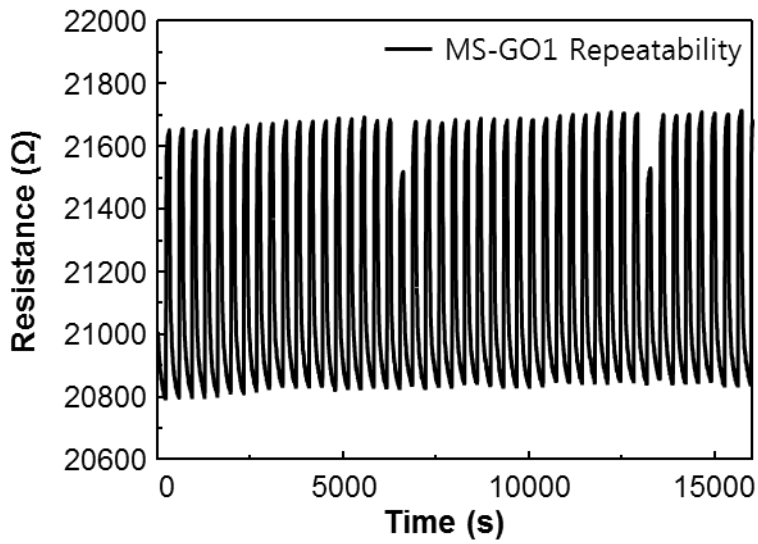

Figure 2.9. Long repeatability to 50 % R.H at 25 ℃

2.3.3. Sensing performance with flexible substrate

The sensing performance of flexible device was examined, which broadens the applications of possibility of MS-GO sensor to wearable devices. PET film was used for substrate of the flexible device and Pt electrodes were deposited on the PET film by E-beam evaporator. To confirm stable sensing performance under bending strain, the flexible device was attached on the pen cap (Figure 2.10a). The bent sensor was transported into the chamber of the sensing measurement system (Figure 2.10b). Figure 2.10c shows the sensing performance of MS-GO2 at 1 V before and after bending (flat and bent). The response of the flat and bent sensor was 43.89 % and 25.01 %, respectively. The sensor was still working owing to the flexibility.

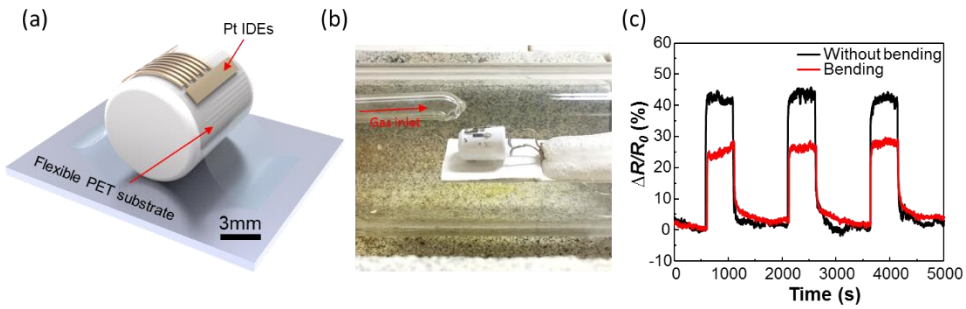

Figure 2.10. Schematic of a bended IDE sensor on a PET substrate. (b) Photograph of humidity sensing setup for the sensor under bending strain. (c) Response curves of the sensor without and with the bending strain.

2.3.4. Gas Sensing Mechanism

The enhanced sensing properties of MS-GOs to humidity is considered to be induced by the following functions. First, the residual oxygen containing functional groups on the surface of rGO make the material more hydrophilic and play a critical role in detecting humidity [69,73,75]. Moreover, the dangling bonds on the edge site of MoS_2 can react with approaching water vapor [28,83,89]. By combination of these two functions, humidity sensing properties of MS-GOs were improved compared to base materials of pristine GO and MoS_2. Second, the mechanism of enhanced sensing properties of MS-GO is illustrated with schematics in Figure 2.11. From the previous study, rGO is considered to be a *p*-type material and MoS_2 as *n*-type material [76,81]. As both two materials are 2D materials, the van der Waals force is formed between them naturally which induces a heterojunction between rGO and MoS_2 [79]. In case of bare rGO, the rGO are used as an electron tunnel. Compared to bare rGO, the heterojunction formed between *p*-type rGO and *n*-type MoS_2 with depletion layer at the interface of rGO and MoS_2 decreases the electron current path [90]. The potential barrier increases at the humidity condition because water vapor adsorbed on the MS-GO acts as an electron acceptor. In short, maximized active sites and electronic sensitization effect induced extremely improved humidity sensing properties of MS-GO.

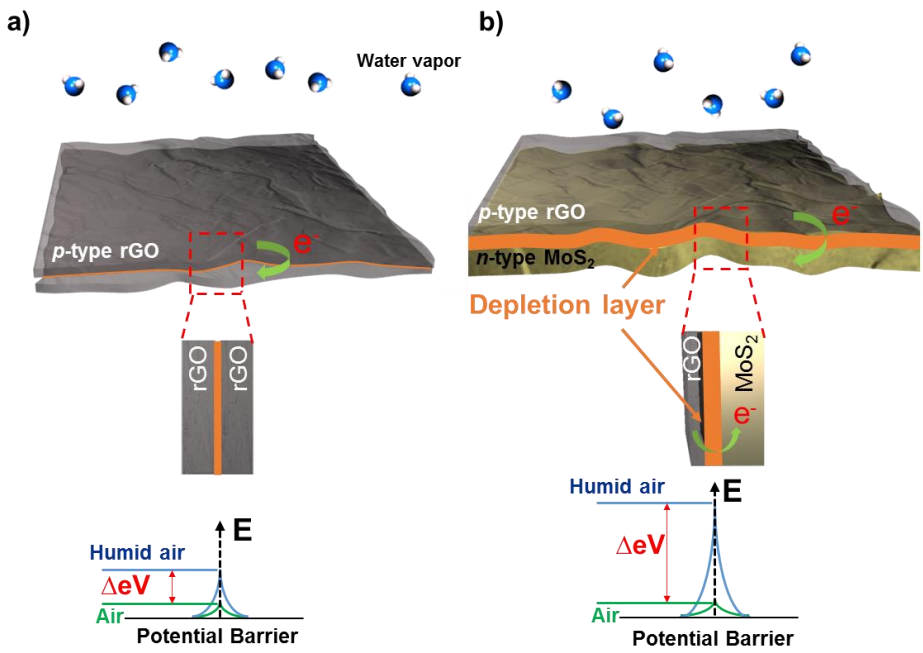

Figure 2.11. Schematic illustration for the current path of rGO and MS-GO. Schematic illustration for the enhanced depletion region on (a) bare rGO and (b) MS-GO.

2.4. Conclusion

We have developed MS-GO based humidity sensors with high response and super-selectivity using simple hydrothermal method. The responses of MS-GO hybrid composites to various gases such as 10 ppm NO_2, 1000 ppm NH_3, 50 ppm H_2, and 50 ppm C_2H_5OH were much increased than those of pristine rGO. Especially, the response to humidity of MS-GO2 was 4 times higher compared to pristine rGO. The theoretical detection limit to H_2O was 178.3 ppm, which demonstrates the encouraging the potential application of MS-GO hybrid composites to control relative humidity that might directly affect our health. These results were due to the utmost utilization of the electronic sensitization by decorating rGO with MoS_2. We strongly believe that our sample is very appropriate to make high performance humidity sensor. We suggest that MS-GO can act as a promising sensing material in next generation to develop enhanced performance of resistive humidity sensors.

Chapter 3

Highly selective and sensitive chemoresistive humidity sensors based on rGO/MoS_2 van der Waals composites

3.1. Introduction

Graphene/TMDC is one of the most spotlighted heterostructure in the last decade [91]. Graphene provides a conductive framework and mechanical support while the TMDC addresses several electrochemical problems by advantage of its attractive chemical properties. Several methods have been studied to fabricated 2D/2D heterostructure such as mechanical exfoliation and aligned transfer, CVD method, and solution-based methods. Mechanically exfoliated and transferred 2D heterostructures shows high quality but there are shortcomings related to its scalability. CVD method requires expensive device and high temperature process [92]. Solution-based methods using ultrasonication are mechanical fracture techniques that can generate hydrodynamic shear force in many types of reactions, material handling, and synthetic cavitation. Sonication can generate nanomaterials by hydrostatic shear, promote the dispersion of MoS_2 and graphene, and obtain the oxidizing effect of -OH, -H, -N, and -O generated during the sonication process. Increased temperature during processing can lead to thermal degradation of volatile hydrophobic materials in the mixed material. The sonication process is very promising because it is simple, environmentally friendly and can be delaminated simultaneously [93]. Sonication not only helps exfoliate bulk materials into nanoscale products in the absence of external reducing agents and reactants, but also disperses MoS_2 and graphene uniformly in the solution or solvent [93–95].

Coleman *et al.* recently reported that MoS_2 nanosheets can be easily obtained by sonicating MoS_2 powders by selecting an appropriate solvent, and that this method can be used to mass-produce MoS_2 nanosheets at low cost [96]. Similarly, uniform graphene nanosheets (single or multilayer) can be obtained simply by sonication in water, providing a new platform for easy production of graphene-based materials. Since both rGO and MoS_2 are 2D materials with layered structures, they can naturally form hetero junction by van der Waals force.[79] Heterostructures between 2D layered materials have recently been reported, and the van der Waals *p*-*n* heterojunction between *p*-type rGO and *n*-type MoS_2 was reported for its application in water splitting electrodes.[83,97] Accordingly, the composites between hydrophilic nature of 2D rGO and 2D MoS_2 with abundant active edge sites can form large area of *p*-*n* heterojunction which is advantageous to enhance humidity sensing performance via controlling electronic transport at the hetero-interface and synergistic promotion of humidity sensing reaction. [76,90,97]

Herein, we report rGO and MoS_2 hybrid composites (RGMSs) based humidity sensors that are unprecedentedly selective to other gaseous molecules at room temperature. The RGMSs were fabricated with very simple process in room temperature with low cost. The sensing properties of RGMSs are dramatically enhanced by a *p*-*n* heterojunction formed between rGO and MoS_2, attributed to the extreme exploitation of the electronic sensitization. The *p*-*n* heterojunction is

clarified by peak shifts in X-ray photoemission spectroscopy (XPS) and Raman spectra.[98,99] We also present the linearity of the sensors for varied humidity concentrations range from 5% to 85% humidity, the theoretical detection limit, and reliable operation upon multiple sensing events. The calculated detection limit was 0.0109% RH. As RGMSs consist of 2D van der Waals materials, the fabrication process is rather simple and free from high temperature annealing, and thus highly flexible humidity sensors are demonstrated by using drop-casting method on gold electrodes deposited on the PET substrate with E-beam evaporator. The flexible humidity sensor showed no degradation in sensing performance after bending several times. The synergistic combination of rGO and MoS_2 indicates that possibility of realizing a humidity sensor for use in wearable electronics.

3.2. Experimental section

3.2.1. Preparation of graphene oxide (GO)

GO was prepared by the modified Hummers method. Briefly, 2 g of graphite powder (Alfa Aesar, 200 mesh, 99.9995 %) was stirred with 2 g of sodium nitrate ($NaNO_3$) and 100 mL of concentrated sulfuric acid (95%) for 1 day in an ice water bath. After the oxidation process, 12 g of potassium permanganate ($KMnO_4$) was gradually added into the reaction mixture. Once it was mixed well, the ice bath was removed, and the solution was stirred at 50 °C until at highly viscous liquid was obtained. After adding 100 mL of de-ionized (DI) water, the suspension was heated

in a water bath at 98 °C for 20 min. Then, it was further treated with warm water and hydrogen peroxide in sequence. The mixed solution was centrifuged at 6,000 rpm and washed with hydrogen chloride (35%) and DI water for removing residual byproducts. The centrifuging and washing process were repeated with five times. Finally, the GO was dried at 50 °C for 24 hours in a vacuum oven.

3.2.2. Reduction of GO

The dried GO sheets were exfoliated by the sonication method. The brown dispersion of GO sheets was centrifuged at 8,000 rpm for 10 min to remove the un-exfoliated GO. The reduction of GO was used by hydrazine hydrate (NH_2NH_2, 50–60% in DI water). The GO solution was mixed with a NH_2NH_2 solution with a ratio of 1 mg of GO to 1 mM of NH_2NH_2 reducing agent. The reduction process was conducted with a water-cooled condenser for 24 h. Finally, the reduced graphene oxide (rGO) solution was successfully obtained after vacuum filtration and washing with acetone.

3.2.3. Fabrication of RGMS hybrid composites

rGO and MoS_2 powder (Graphene market) were separately dispersed in 2 mL DI water by ultra-sonication at 60 Hz for 10 min. To make RGMS, the molecular weight of rGO and MoS_2 were set to 12 and 160.07 g/mol each, and the molar ratio was calculated to be 1:1, 1:5, and 1:10 for RGMS 1, RGMS 5, and RGMS 10,

respectively. The calculated amounts were mixed and re-dispersed by ultra-sonication for 24 h to make mechanical interaction between rGO and MoS_2.

3.2.4. Sensor fabrication

Inter digitated electrodes (IDEs) with an interspacing of 4 μm was prepared on SiO_2/Si substrate by photolithography followed by metal (Pt/Ti) deposition by e-beam evaporation. A 0.4 μL drop of RGMS was cast onto a Pt IDE/SiO_2/Si substrate and dried for 10 min at 100 °C to remove DI water.

3.2.5. Characterization

The surface morphology and the microstructure of the fabricated RGMS on the Si substrate were characterized by a field-emission scanning electron microscopy (MERLIN Compact, ZEISS) using 1kV. Energy dispersive spectroscopy (EDS) mapping was carried out on RGMS in the scanning SEM mode. For the transmission electron microscopy (TEM), RGMS were deposited on a quantifoil Cu grid (300 mesh holey carbon). The TEM experiments were performed using a JEM-2100F spectrometer. Also, EF-TEM was performed for RGMS. Raman scattering was performed using a Raman spectrometer at an excitation wavelength of 532 nm using laser light. XPS was carried out at Research Institute of Advanced Materials in Seoul National University. Ultraviolet photoelectron spectroscopy (UPS) was performed to confirm the creation of p-n junction between rGO and MoS_2 by clearly showing the band structure of rGO and MoS_2. Electrochemical

impedance spectroscopy (EIS) was conducted from 10 kHz to 10 mHz with an AC amplitude of 10 mV. The measured spectra were fitted by using the ZSimpWin software.

3.2.6. Sensor measurement

Gas sensing properties of RGMS sensors were measured in a quartz tube at room temperature by monitoring the variation of sensor resistance on flowing dry air to a calibrated humid air (balanced with dry air). The response of RGMS was accurately determined by measuring the base resistance in dry air and the fully saturated resistance after exposure to humid air. The sensor resistance was measured at a DC bias voltage of 1V using a source measurement unit (Keithley 236). A constant flow rate of 500 sccm was used for dry air and the humid air. The response of the RGMS sensors was precisely determined by the ratio of the fully saturated resistances after exposure to the humid air to the base resistances in dry air

3.3. Result and discussion

3.3.1. Fabrication process and electrical properties

RGMSs were synthesized by a simple process. The fabrication process of RGMSs is demonstrated in Figure 3.1. rGO and MoS_2 were soaked in distilled water and dispersed by ultra-sonication for 10 min. Dispersed rGO and MoS_2 were added together with 1:1, 1:5 and 1:10 molar ratio of rGO:MoS_2 and the samples were

named as RGMS 1, RGMS 5 and RGMS 10 each. The molecular weight of rGO and MoS_2 are considered to be 12 and 160.07 g/mol. After mixing rGO and MoS_2 together, ultra-sonication was used for 24 h to uniformly bind together. During the synthesis process of RGMSs, thermal annealing process or chemical agent that might affect the original characteristics of rGO and MoS_2 were not used. After ultra-sonication, 0.4 μL of slurry containing RGMS was deposited on the Pt interdigitated electrodes (IDEs) with an active area of 1 mm × 1 mm with 4 μm interspace. After drop-casting, the IDE was fully dried to evaporate distilled water. Figure 3.2a shows the scanning electron microscopy (SEM) image of a RGMS, confirming that rGO in the net form and MoS_2 in layered structure are attached together. The SEM images of pristine rGO, MoS_2, RGMS 1 and RGMS 10 are shown in Figure 3.3 to compare with RGMS 5. To confirm the existence of rGO and MoS_2 in a RGMS, energy dispersive spectroscopy (EDS) mapping was carried on the RGMS. For EDS mapping, area was selected randomly, and the selected area is shown in Figure3.2b. Figure 3.2c, d, e, and f show the element mapping of Mo, S, C, and O respectively, for the selected area in Figure 3.2b, indicating the co-existence of Mo, S, C, and O. This suggests that MoS_2 is well attached on rGO with no serious aggregation. In addition, Figure 3.3a shows rGO sheet which can wrap MoS_2 by continuous sonication. By this phenomenon, element mapping of Mo, S, C and O shows signal at same position. The oxygen shown in EDS mapping is from the oxygen containing functional groups at the defect site of rGO.[100]

Figure 3.4a and b show the TEM images of RGMS. Figure 3.4a shows the TEM image of a RGMS, indicating that the rGO and MoS_2 co-exist by checking the interlayer distance of MoS_2 in RGMSs, corresponding to the pristine MoS_2. The SAED pattern shown in the inset of Figure 3.4b indicates the presence of various planes of MoS_2 ((100) and (110)). In addition, the TEM image of pristine rGO and MoS_2 are shown in Figure 3.3e-h. The amorphous characteristics of rGO and crystallinity of MoS_2 are revealed in the inset in Figure 3.3f and h respectively. Moire patterns in Figure 3.3h indicates overlapping phenomenon of different MoS_2 planes with an interlayer distance of MoS_2 as 0.27 nm between (100) plane and 0.16 nm between (110) plane (MoS_2 JCPDS No.: 37-1492). From this TEM image, the morphology of RGMS is clearly confirmed. The wettability of pristine rGO, RGMS 5, and pristine MoS_2 were also revealed by their static contact angle with water (Figure 3.5a, b, and c). The same amount of water droplets (0.5 μL) was dropped onto the rGO, RGMS 5, and MoS_2 at the same time. The static contact angle between rGO and water was found to be 41.2°. Hence, rGO shows a good hydrophilicity property, and the oxygen containing groups presumably exist on the surface of rGO. The contact angle between MoS_2 and water was 44.2°. Compared to the pristine rGO and MoS_2, RGMS 5 showed a higher hydrophilicity of 36.9°. The water droplet on rGO and MoS_2 remained, but the surface of water droplet on RGMS 5 spread out, indicating increased hydrophilicity of RGMS 5 compared to those of the pristine rGO and MoS_2.

To determine the existence of rGO and MoS_2, Raman spectrum of RGMS 5 was compared to those of MoS_2 and rGO (Figure 3.6e and f), confirming that the MoS_2 and rGO are well hybridized. The gap between the peaks for in-plane (E^1_{2g}) and out-of-plane (A_{1g}) vibrational modes shows the number of MoS_2 layers. Compared to pristine MoS_2, both peak of the E^1_{2g} and A_{1g} in RGMS have blue shift (E^1_{2g} from 379.72 to 377.00 and A_{1g} from 405.72 to 403.00 cm^{-1}) maintaining same gap width of 2.72 cm^{-1}, which means that the MoS_2 in RGMS has same number of layer with pristine MoS_2. The blue shift means that lattice vibration modes in MoS_2 in the composite need more energy than those in the pristine MoS_2 since MoS_2 is anchored by rGO in the composite.

This is an evidence of van der Waals heterojunction between rGO and MoS_2. On the other hand, there is no considerable peak shift in D and G peaks for the pristine rGO and RGMS 5. MoS_2 is surrounded by rGO, but most of the surface of rGO is not contacted with MoS_2. It is considered that the decreased intensity of D and G peaks of RGMS is due to the fact that MoS_2 interrupts the layer-by layer stacking of rGO in composite as seen in Figure 3.1.

The D and G peak of rGO are shown at 1345.0 and 1587.0 cm^{-1}. The D peak of rGO is attributed to the sp^3 defect sites, and G peak indicates the existence of sp^2 carbon atoms with in-plane vibrations (E^1_{2g}). According to the decreased intensity of D-band, superior device performance is expected because low energy binding

sites such as carbon sp^2 bonds cause fast gas reactions and high energy binding sites such as point defects provide slow gas reactions. As the surface of rGO decreases due to the contacted area with MoS_2, the intensity of D and G peaks in RGMS is relatively decreased. [75,84,89]

The XPS spectra of RGMS 5, the pristine rGO and MoS_2 (Figure 3.6a, b, and c) were compared to investigate the chemical state of Mo and S. The XPS spectrum of the pristine MoS_2 shows five main peaks including the 2s of MoS_2 peak at 226.5 eV. The four main peaks of Mo $3d^{4+}_{5/2}$, Mo $3d^{4+}_{3/2}$, Mo $3d^{6+}_{5/2}$, and Mo $3d^{6+}_{3/2}$ at 229.3, 232.4, 233.1, and 235.6 eV, respectively, are the characteristics of MoS_2. The XPS spectra of sulfur edges in MoS_2 show the $2p_{1/2}$ and $2p_{3/2}$ core levels at 162.1 and 163.3 eV each (Figure 3.6b), which is consistent with the previous reports.[101] Since rGO has sp^2 carbon with pi-electrons, which determine the physical and electrical properties of rGO, the portion of sp^2 bonding can provide the hint of structure–property relationships.[72] As shown in Figure 3.6d, the C 1s XPS spectrum of rGO shows the four different carbon atoms in different functional groups, indicating the existence of the following oxygen functional groups: C–C at 284.4 eV, C–OH at 285.1 eV, C–O at 286.1 eV, and C=O at 287.5 eV. As for RGMS 5, the binding energies slightly increased compared to those of pristine MoS_2 and rGO. The binding energy of Mo 3d in RGMS 5 shown in Figure 3.6a

indicates that Mo $3d^{4+}_{5/2}$, Mo $3d^{4+}_{3/2}$, Mo $3d^{6+}_{5/2}$, and Mo $3d^{6+}_{3/2}$ increased to 229.4, 232.5, 233.1, and 235.7 eV.

Binding energy of the principal peaks of S 2p (S $2p_{1/2}$ and S $2p_{3/2}$) in RGMS 5 increased to 162.3 and 163.5 eV each (Figure 3.6b). Moreover, the binding energy of C 1s with C–C, C–OH, C–O, and C=O peak also showed slight increase to 284.5, 285.2, 286.2, and 287.6 eV for RGMS 5 (Figure 3.6c). All these results indicate the interaction between rGO and MoS_2 in RGMS 5, allowing electron transfer between the connection of rGO and MoS_2. This phenomenon can significantly affect the conductivity of RGMS. Theoretically, atom contains the inner electrons, outer electrons, and nucleus. Coulomb interaction exists between the inner electrons and nucleus, and the outer electrons carry out shielding effect to the inner electrons, indicating that as the concentration of the outer electron decreases, the shielding effect relatively decreases, and thus increase the binding energy of the inner electrons for the existence of penetration effect, resulting in the corresponding XPS peaks shift to a higher energy direction. Clearly, the XPS surveys in Figure 3.6 show that electrons can transfer from MoS_2 to rGO, and this can be the evidence of heterojunction formation.[84] Moreover, the ratio of the bonding state in rGO with C=C, C–C, C–O, and C=O is shown in Figure 3.6d. The ratio of the bonding state of RGMS is observed at almost the same inclination to rGO.

To observe the electronic structures of RGMS heterojunction, UPS analysis was performed. The work function can be calculated from the energy difference between the Fermi level and the vacuum level. The valence band maximum can be calculated from the difference of the lowest binding energy. As shown in the Figure 3.7a, after forming composite, the work function of the rGO has decreased from 4.65 to 4.60 eV and MoS_2 has increased from 4.55 to 4.60 eV. In Figure 3.7b, the energy difference between the Fermi level and valence band maximum is increased, demonstrating the *n*-type behavior of MoS_2 and decreased indicating *p*-type behavior of rGO. On the basis of the results, we have made a band diagram indicating the band bending behavior at the interface of rGO and MoS_2 (Figure 3.3c and d).[102,103]

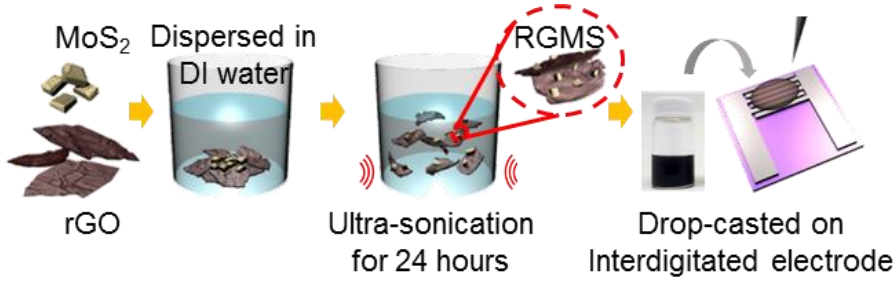

Figure 3.1. Fabrication procedure of rGO@MoS_2 humidity sensor.

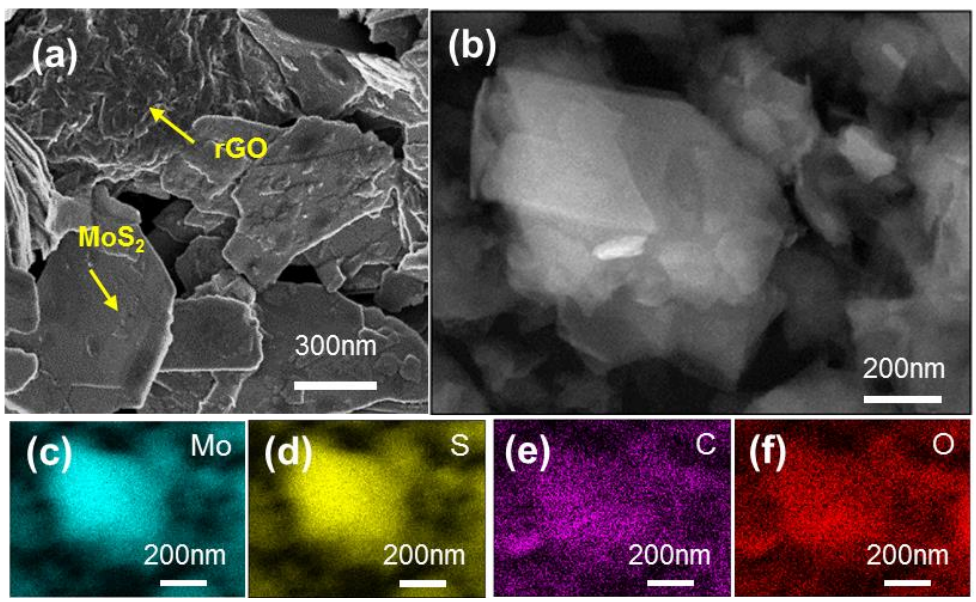

Figure 3.2. (a) SEM image of RGMS. (b) EDS spectrum of RGMS. (c) Molybdenum, (d) sulfur, (e) carbon, and (f) oxygen elemental mapping of RGMS.

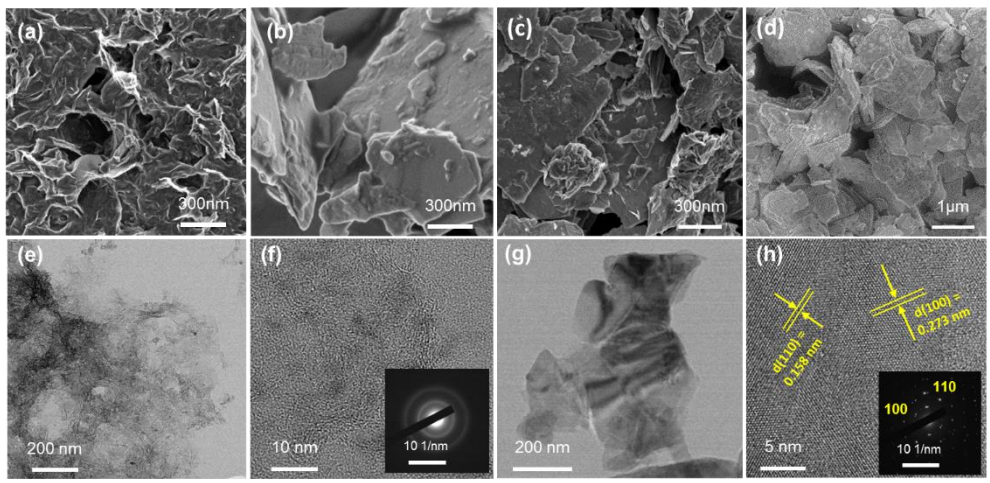

Figure 3.3. SEM images of (a) rGO, (b) MoS_2, (c) RGMS 1 and (b) RGMS 10. And TEM images of (e) rGO and high-magnification TEM image of rGO. TEM image of (e) MoS_2 and (h) high-magnification TEM image of MoS_2**.**

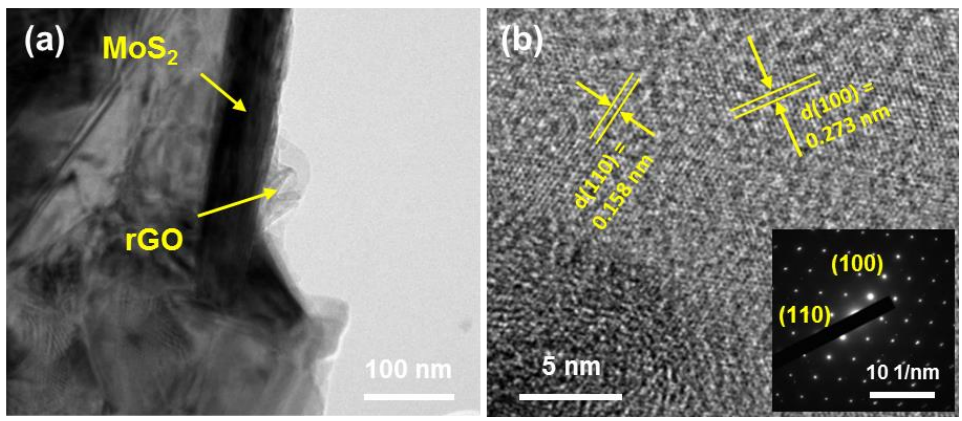

Figure 3.4. HRTEM images of RGMS with (a) low resolution and (b) high resolution.

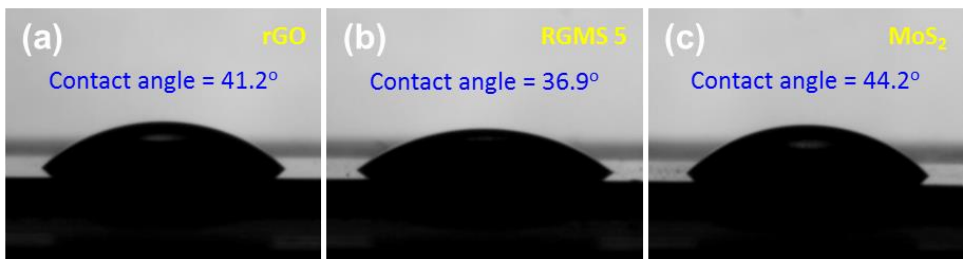

Figure 3.5. Surface tension of water drops on (a) rGO, (b) RGMS 5 and (c) MoS_2.

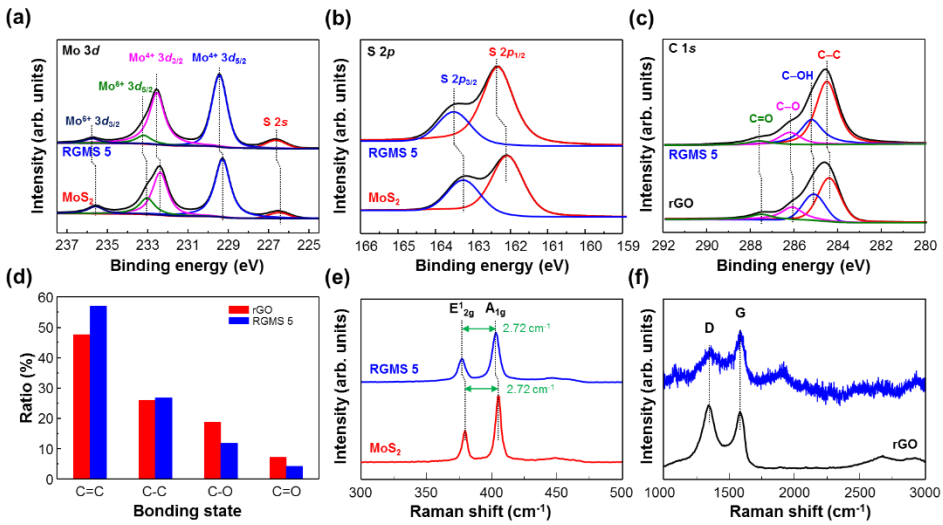

Figure 3.6. Raman spectra of rGO, MoS_2 and RGMS. XPS spectra of RGMS compared with rGO and MoS_2. (b) Mo 3d, (c) S 2p, (d) C 1s and (e) the ratio of bonding state

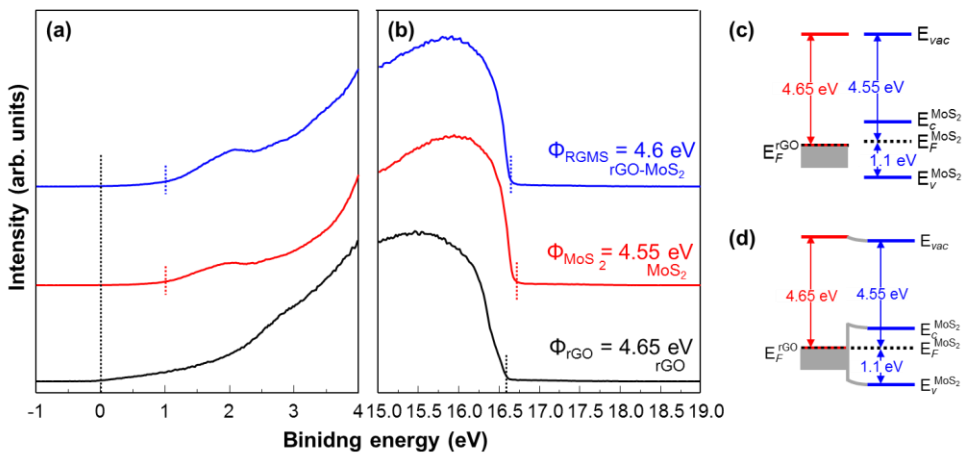

Figure 3.7. UPS spectra of MoS_2, rGO and RGMS. (a) HOMO and (b)the secondary electron cutoff. Band diagram of RGMS heterojunction at (a) flat band condition and (d) equilibration of Fermi.

3.3.2. Gas sensing properties of MS-GO

For the comparison of humidity sensing property, pristine rGO, RGMS 1, RGMS 5, RGMS 10, and MoS_2 were drop casted on IDE for the sensing measurements. Figure 3.8a shows the dynamic sensing transient of pristine rGO, MoS_2, RGMS 1, RGMS 5, and RGMS 10. The device was exposed to three consecutive pulses of 500 sccm of humid air balanced with dry air (Figure 3.8a). The response of the samples is defined by the following equation: $(R_{humidity} - R_{air})/R_{air} \times 100$ where R_{air} and $R_{humidity}$ denote the resistance in the dry air and humid air, respectively. The responses of pristine rGO and MoS_2 are 4.1 and 70.7%, respectively. All the RGMSs showed increased response compared to the pristine rGO. RGMS 1, RGMS 5, and RGMS 10 showed 10.5, 872.7, and 86.6% of response each (Figure 3.8b). The error bars indicate the maximum and minimum values of response obtained from three sensors of each MoS_2 at given concentration which are exposed to 50% R.H (Figure 3.8b). RGMS 5 shows a dramatic enhancement in response, exhibiting 220 times higher than that of pristine rGO.

The base resistance increased with increasing molar ratio of MoS_2 (Figure 3.9). Pristine rGO showed conducting properties with a base resistance of 52.2 Ω and MoS_2 showed insulating characteristic showing its base resistance of 3.1×10^8 Ω. As the base resistance increases, the noise in the measurement also increases relatively. To have exceptional chemoresistive properties, the resistance of the gas

sensing device has to be in optimal range. The noise signal of MoS_2 is due to the exceeding resistance range of reading capability of the measurement unit.[103] Therefore, controlling the base resistance of the sensing material is an important factor for humidity sensor. In the inset of Figure 3.8b, all the mixed samples showed different baseline resistances in the ambient air. The baseline resistance of the RGMS 1, RGMS 5 and RGMS 10 increased relatively with increasing mole fraction of MoS_2 (1.6 kΩ, 11.8 kΩ, and 9.5 MΩ each shown in Figure 3.9b, c, and d). As the rapid increase of the resistance around 83.3% of MoS_2 concentration, the critical threshold of percolation is considered to be 83.3% of MoS_2 concentration. Therefore, the composites containing 16.7% or less of rGO shows a sensitive resistivity increase by the molar concentration of the insulating phase. The slight increase of base resistance of the RGMSs containing higher than 17% concentration of rGO can be explained by conducting path formed by rGO.[104,105]

Figure 3.10a shows the responses of RGMS 5 to 50% R.H, 50 ppm H_2, 50 ppm CH_3COCH_3, 10 ppm NO_2, and 1000 ppm NH_3 at 27 °C, 1V. The response ($|\Delta R/R_0|$) of RGMS 5 to 1000 ppm H_2, 50 ppm CH_3COCH_3, 10 ppm NO_2 and 1000 ppm NH_3 is 3.2, 17.8, 29.6 and 47.9%, respectively. The RGMS 5 based sensor showed the highest response to 50% R.H (~873.7%). The dynamic sensing transients of RGMS 5 are shown in the inset of Figure 3.10a, indicating that RGMS 5 has extremely high selectivity to humidity, which is one of the most critical factors of

semiconductor sensors. In previous study, pristine rGO and MoS_2 shows high selectivity to NO_2.[46,69] According to the previous researches, more than 10 ppm of NO_2 and out of the range of 30-60% of R.H has a detrimental effect on human body. The RGMS 5 sensor showed 30 times higher sensitivity at 50% R.H than at 10 ppm NO_2. For the practical applications, high stability upon multiple repeatability is required for humidity sensor. The RGMS 5 sensor showed excellent repeatability as shown in Figure 3.10b. Three of RGMS 5 sensors were fabricated and the sensing properties of each samples were measured 4, 12, and 20 months after fabrication. RGMS 5_1, RGMS 5_2 and RGMS 5_3 showed 658.24, 846.87 and 1609.27% of response each immediately after the sensors were fabricated. The sensors still showed 846.87, 907.51 and 1328.30% of response respectively after 4, 12 and 20 months. RGMS 5 was repeatedly exposed to 50% R.H at 27 ℃, as shown in Figure 3.10c. After multiple exposures to 50% R.H, RGMS 5 recovered its original baseline resistance.

To evaluate the humidity response linearity and calculate the detection limit of RGMS 5 at 27 ℃, the response of the sensor was measured in the range from 5% to 85% R.H, as shown in Figure 3.10d. Electrical impedance spectroscopy (EIS) was measured in order to determine gas reaction in RGMS humidity sensor. The Nyquist plots of the RGMS are shown in Figure 3.11a. The equivalent circuit of R_2 shown in Figure 3.11b and c represents the interfacial resistance between the

sensing material and the ambient air conditions (dry and humid conditions), and R_3 represents the resistance between the adsorbed water molecules on the surface of RGMS and dry air. From the impedance fitting, the R_2 under dry condition was measured to be 29413 Ω and the resistance under humid condition was 41816 Ω.[106] The increased response values with increasing humidity concentration can be explained by the Grotthuss Mechanism.[107] Previous studies have shown that at low concentration of R.H, water molecules are physisorbed by forming two hydrogen bonds at the active sites such as hydrophilic groups, and vacancies.[108,109] At this point, the water molecules are not able to move because of the formation of the two hydrogen bonds. Therefore, significant energy is required for proton to transfer between the adjacent –OH groups of the first layer physical adsorption of water, resulting in strong electrical resistance. As the R.H increases, multilayer physical adsorption of water molecules is formed. In the second physisorbed layer, water molecules move easily, because of the formation of just one hydrogen bond. Moreover, in multilayer physical adsorption progress, physisorbed water molecules are ionized by an electrostatic field to form a large number of H_3O^+, acting as the charge carrier. At higher R.H, physisorbed water layers show liquid like behavior. In the bulk liquid, charge transport occurs by the Grotthuss chain reaction ($H_2O+H_3O^+ \rightarrow H_3O^+ + H_2O$), as proton hopping occurs between the adjacent water molecules. Moreover, at high R.H, physisorbed water penetrates between the RGMSs and interacts with the functional groups of RGMSs, affecting the ionic

conductivity. This phenomenon is caused by electron conduction through the RGMSs sensing channel and proton hopping through the continuous water layer following the Grotthuss mechanism. The values of response were plotted as a function of the humidity concentration as shown in Figure 3.10d. A linear regression fit was applied to find out the relationship between the responses and the concentrations of humidity. The linear regression equation is indicated as y = 28.4x - 127.0. In this equation, x is the humidity and y is the response value. The measure of goodness-of-fit of the linear regression, r^2, was calculated to be 0.104. The responses of the sensor are 174.2, 541.2, 965.2, 1590.6, and 2494.3% at 5, 25, 45, 65, and 85% of R.H. To get different humidity condition, 5% R.H was controlled with 50 sccm humidity/950 sccm air, 25% R.H with 250 sccm/750 sccm, 45% R.H with 450 sccm /550 sccm, 65% R.H with 650 sccm/350 sccm and 85% R.H with 850 sccm/150 sccm. The lowest measurable humidity on the equipment used in this study was 5% R.H; however, the theoretical detection limit was calculated to be 0.0109% R.H.[98,99] In addition, Figure 3.10f shows the hysteresis curves of the sensor device in the process of adsorption and desorption. The humidity level was ranged from 5-85% R.H with ascending R.H from 5% to 85% (adsorption) and descending R.H from 5% to 85% (desorption). As seen in Figure 3.10f, the two curves are very close. The largest humidity hysteresis is only 5.6% R.H which indicates that the hysteresis for the RGMS 5 humidity sensor is small. The extremely high selectivity, excellent repeatability, and low

concentration of the detection limits to humidity suggest its possibility of practical application to various fields such as industrial automation, pharmaceuticals, agriculture, and environmental monitoring. Moreover, the highest response of the humidity is as high as 2494.2%, which is much higher than those of the humidity sensors for high performance in previous studies using graphene synthesized by the chemical vapor deposition (CVD) method, PDDA/GO, graphene with thermally exfoliated, MoS_2 sheets, and rGO (Table 3.1). While RGMSs showed reversible characteristics, humidity sensors based rGO, graphene and MoS_2 sheets exhibited irreversible sensing properties.[46,61,63,88,110–112] This remarkable response of RGMS is attributed to the *p-n* heterojunction formation between rGO and MoS_2. As described in the table, RGMS 5 shows a high level of response time, recovery time, and response.

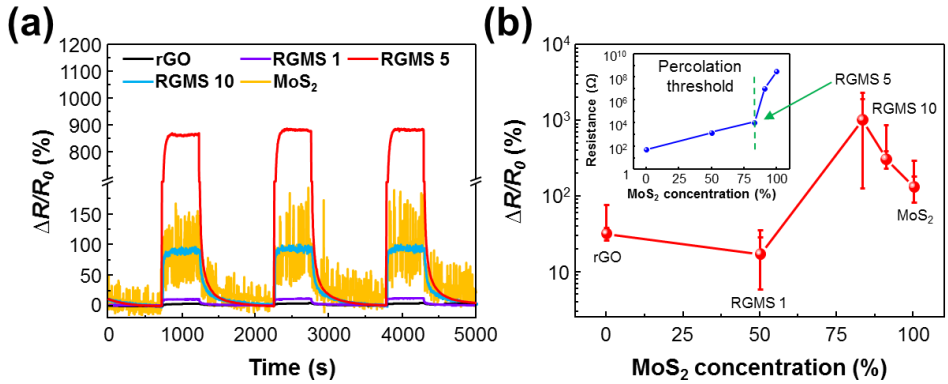

Figure 3.8. (a) Response (($R_{humidity}$− R_{air})/R_{air}) curves of rGO, RGMS 1, RGMS 5, RGMS 10 and MoS_2 to 50% R.H. at 27 °C. (b) Response of rGO, RGMSs and MoS_2 and inset is the baseline resistance of rGO, RGMSs and MoS_2.

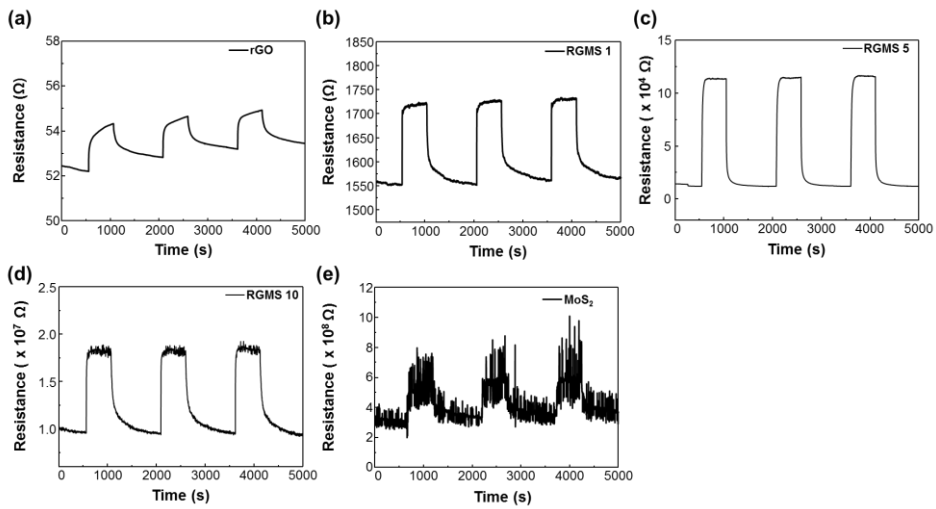

Figure 3.9. Response curves of (a) pristine rGO, (b) RGMS 1, (c) RGMS 5, (d) RGMS 10 and (e) pristine MoS_2 to three pulses of 50% RH at room temperature.

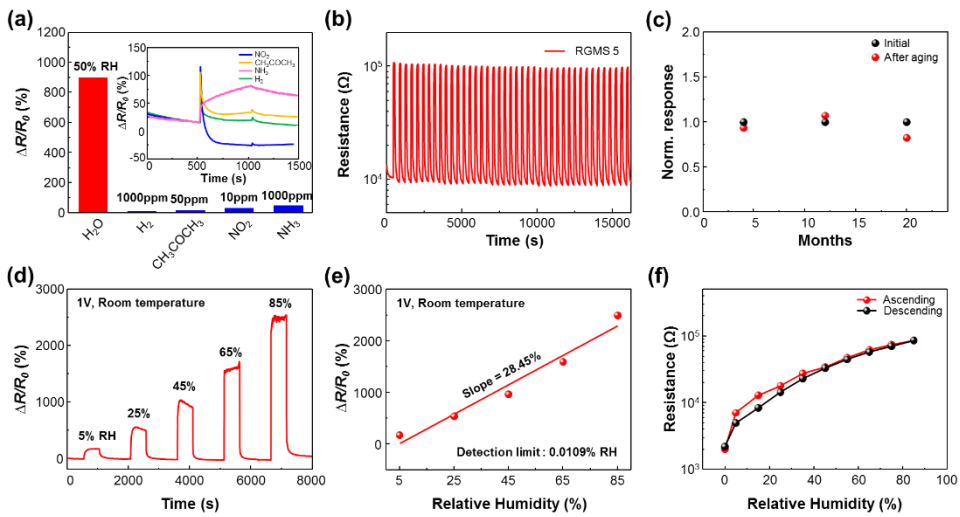

Figure 3.10. (a) Response to various types of gases and inset is the sensing curves of each gases (H_2, CH_3COCH_3, NO_2 and NH_3). (b) Multiple repeatability of RGMS 5 to 50% R.H. (c) Long term stability of RGMS 5 with three different samples with 4, 12 and 20 months respectively. (d) Response curves to different RH of 5%, 25%, 45%, 65%, and 85% at 1V. (e) Linear fit of the responses as a function of humidity air at 1V. (f) Hysteresis of RGMS 5 at different R.H of 5%, 25%, 45%, 65%, and 85% at 1V.

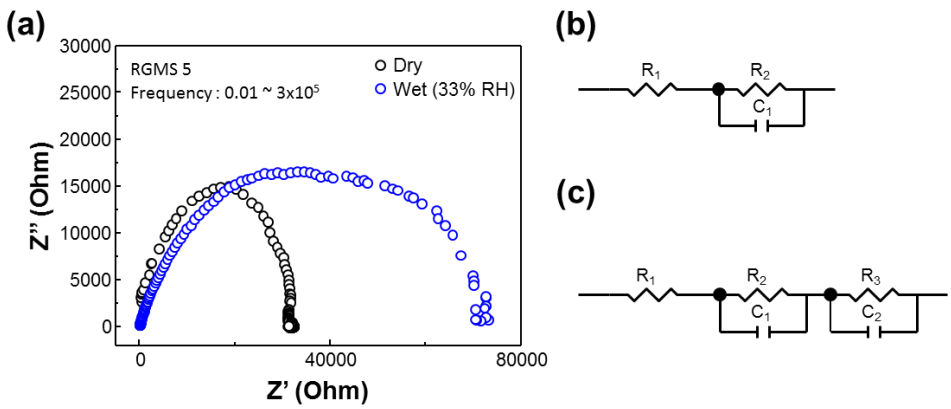

Figure 3.11. (a) Nyquist plots of RGMS 5 in dry air and wet air condition. Equivalent circuits of RGMS 5 under (b) dry air condition and (c) wet air condition.

3.3.3. Sensing performance with flexible substrate

The sensing performance with a high bending strain was also investigated to broaden the applications of RGMS-based humidity sensor to wearable devices. Thin PET film was used for the flexible substrate, and Pt electrode was deposited on the thin PET film with E-beam evaporator (Figure 3.12a). To validate stable sensing operation under bending strain, the flexible substrate was attached on the pen cap (bending radius of 7mm). The bent sensor was loaded to the chamber of the humidity sensing measurement device (Figure 3.12b). Figure 3.12c shows the sensing curves of RGMS 5 without and with the bending strain (flat and bent). Before bending, the sensor showed the 1484.7% of response to 50% humidity. When the sensor was bent, the sensor still worked owing to the high flexibility of RGMS showing the 1506.32% of response. This can make RGMS 5 applicable to various fields, typically wearable device and health care.

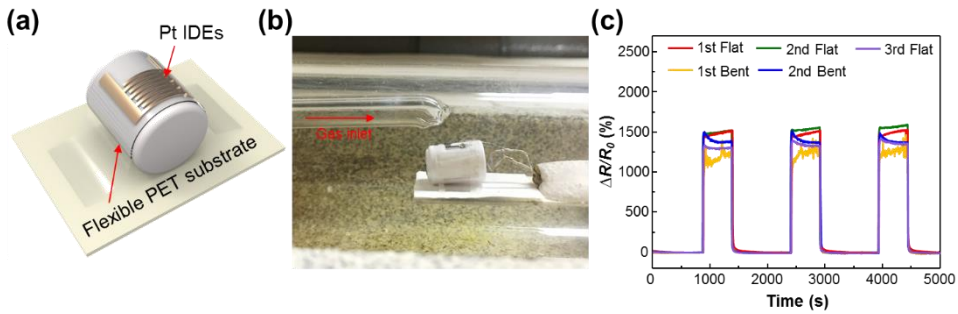

Figure 3.12. (a) Schematic of a bended IDE sensor on a PET substrate. (b) Photograph of humidity sensing setup for the sensor under bending strain. (c) Response curves of the sensor without and with the bending strain.

3.3.4. Gas sensing mechanism

The enhanced humidity sensing properties of RGMSs are attributed to the following factors: the utility factor, receptor function, and transducer function. First, the structural characteristics of RGMSs provide a large surface area and high hydrophilicity, indicating that the water vapor can be adsorbed by the oxygen containing functional groups on the surface of rGO and dangling bonds on the edge sites of MoS_2. Therefore, highly sensitive and fast response time was obtained (receptor function).[113] Second, taking MoS_2 as percolating agent through a matrix of rGO sheets, the value of critical number fraction can maximized since the small volume ratio of a MoS_2 and a rGO sheet which shows percolation threshold in the inset of Figure 3.8b. rGO and MoS_2 are considered to be exist forming in rotation demonstrated in Figure 3.13. At the specified concentration of rGO and MoS_2 with maximized active sites, the accessibility of water vapor into RGMSs extremely increases (utility factor).[63,104] For the last, the *p*-*n* heterojunction between rGO and MoS_2 is the principle factor in the enhanced response of composites. In a previous study, 2D materials such as rGO and MoS_2 can naturally form a hetero junction by van der Waals force.[79] As rGO is an inherently *p*-type 2D material and MoS_2 is well known *n*-type material, they can form heterojunction naturally.[76,81] Unlike rGO, which is used as an electron transfer path, RGMS forms a *p*-*n* heterojunction at the interface of rGO and MoS_2 and reduces the electron current path. Since water

vapor acts as an electron acceptor, the potential barrier increases when water molecules adsorb on RGMSs. The modulation of interfacial potential barriers by exposure to wet air was significantly higher in RGMSs than in rGO, increasing the sensing performance (transducer function). In short, maximized active sites, easy accessibility of humidity and electronic sensitization effect induced extremely increased humidity sensing properties of RGMSs which have not been reported yet.

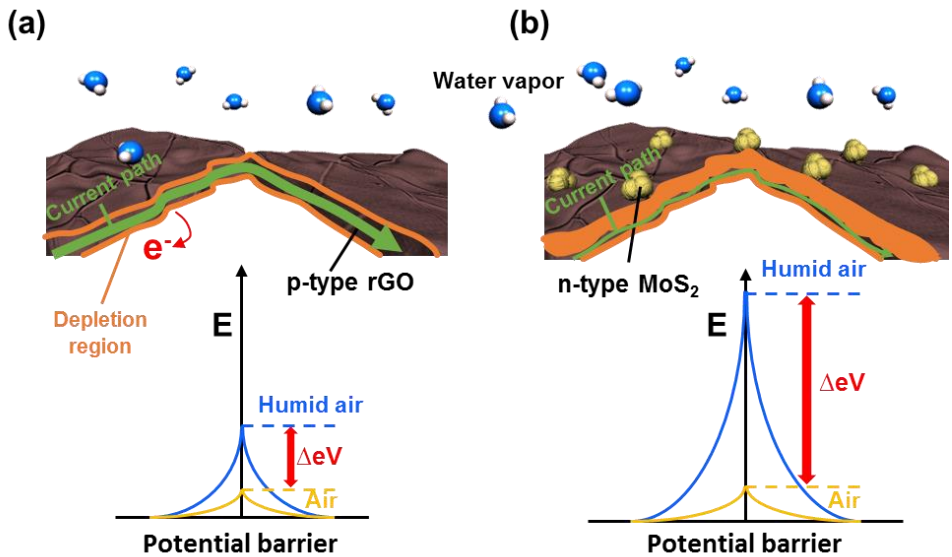

Figure 3.13. Schematic illustration of the mechanism with enhanced humidity sensing properties of the enhanced depletion region on (a) bare rGO and (b) RGMS.

3.4 Conclusion

In conclusion, we developed an RGMS humidity sensor with enhanced sensitivity by a simple fabrication process. RGMS humidity sensor demonstrated high response with long stability and flexibility. The high response of RGMS humidity sensor is attributed to the *p*-*n* heterojunction formed by *p*-type rGO and *n*-type MoS_2 and the effect of the oxygen functional groups remaining on the surface of rGO. We expect that the excellent properties demonstrated in this study have shown the possibility of RGMS-based humidity sensors in practical applications.

Chapter 4

Highly selective noble metal decorated MoS_2 based gas sensor array

4.1. Introduction

The electronic nose (E-nose), which mimics the function of the mammalian olfactory system[1,114–116], is an advanced and promising technology that can substitute human sensory panels for specific purposes in practical applications. By using a chemical gas sensor array in combination with a classification algorithm, e-nose can detect and recognize odors and flavors. E-nose has gained worldwide attention for its critical role in health care[2,4], environmental monitoring[3,14–16], food processing[7–13], security and public safety[6], transportation and industrial processes[2,117]. Since the main purpose of e-noses is to maintain a safe environment for human life, e-nose must be a device that can be integrated with mobile devices or wearable devices that are closely used in human life. Therefore, e-nose should be portable, compact and reliable[6,118–124]. In this respect, semiconductor gas sensors are ideal candidates for applications. Based on the Micro Electro Mechanical Systems (MEMS) platform, e-nose can be operated with very low power consumption by miniaturizing a device consisting of a gas sensing material and a heater in the sensor chip[125].

Two-dimensional (2D) materials including graphene, transition metal dichalcogenides (TMD), and boron/carbon nitride have attracted great attention as gas sensing materials due to their excellent electrical, mechanical and surface properties.[126] 2D gas sensing materials have the advantage of being sensitive to

low concentrations of gases due to their high surface-to-volume ratios. In addition, facile surface modification with charge-transfer doping effects readily improves the gas sensing properties. Among them, TMD is a very suitable material for gas sensors because of its high surface-to-volume ratio and many dangling bonds in edge sites and basal planes that can detect sensitive gases at low concentrations.[46,51,127–130] Since the selectivity of individual materials is limited, methods for improving the selectivity and gas sensing properties of materials have been studied. The methods include nanostructure fabrication and surface decoration to improve selectivity and gas sensing properties. In particular, the fabrication of nanostructures increases the surface area of the material that can react with the gas, increasing sensitivity. Attention has also been paid to methods of improving sensitivity and selectivity through the effect of catalysts containing platinum, palladium and gold nanoparticles. MoS_2 is easy to incorporate surface adatoms such as noble metal nanoparticles on the surface due to the functional groups present at the edge site and basal plane. This feature induces electron exchange between the 2D material and the metal nanoparticles decorated on the surface, resulting in doping of the 2D material.

Herein, we provide the effects of Au, Pd and Pt incorporation on MoS_2 were investigated. Incorporation with Au, Pd and Pt significantly improves the chemical sensing ability of the MoS_2 system. During the solution mixing of an aqueous

solution of $HAuCl_4$, K_2PdCl_4 and K_2PtCl_4, the metal precursors were reduced as a result of the charge transfer of electrons from the MoS_2 flakes, which were subsequently incorporated into the MoS_2 surface because of the difference in the reduction potential between the Au (or Pd or Pt) precursors and the MoS_2 work function and they were characterized through Scanning electron microscope (SEM), Transmission electron microscopy (TEM), raman and X-ray photoemission spectroscopy (XPS) analysis. The pristine, Au-decorated, Pd-decorated and Pt-decorated MoS_2 ($PMoS_2$, Au-MoS_2, Pd-MoS_2 and Pt-MoS_2) were exposed to six different gases at 150 °C to evaluate their gas sensing behavior. This study also presents a classification of gas component using Principle Component Analysis (PCA). Finally, the selectivity of each materials is proved by first-principles density functional theory (DFT) calculation. This study provides clear understanding on the effect of noble metal catalysts on improving gas sensing selectivity by MoS_2 which can be applicable into e-nose.

4.2. Experimental section

4.2.1. Fabrication of metal nanoparticles on MoS_2

3 mg of layered MoS_2 powder (~90 nm powder, 99% purity, 5g; Graphene supermarket) was dispersed in a 45 vol % ethanol/water mixture (1ml/mg) and sonicated in an ultra-sonication bath for several hours. In an individual vial, gold chloride monohydrate ($HAuCl_4 \cdot H_2O$), potassium tetrachloropalladate (K_2PdCl_4),

and Potassium tetrachloroplatinate (K_2PtCl_4) was dissolved in water. To decorate MoS_2 with Au, Pd, and Pt nanoparticles, a small amount of the $HAuCl_4$, K_2PdCl_4, and K_2PtCl_4 solution was added each vial to an aqueous dispersion of chemically exfoliated MoS_2 at specific temperature, which was then stirred for several minutes. A reaction occurred immediately, completing within a few minutes.

4.2.2. Sensor fabrication

IDEs of 4 μm interspacing were prepared on SiO_2/Si substrate using photolithography followed by metal (Pt/Ti) deposition by e-beam evaporation. A 2 μl drop of MoS_2 nanoparticle solution was cast onto a Pt IDEs/SiO_2/Si substrate and was then dried for 30 minutes at 100 °C. The fabricated sensors were calcined at 500°C in Ar ambient to crystallize the noble metal nanoparticles using Rapid Thermal Annealing (RTA).

4.2.3. Characterizations

Noble metal decorated MoS_2 on Si substrate were characterized by a scanning electron microscope (FE-SEM, MERLIN Compact, ZEISS) using 5 kV. For TEM analysis, noble metal decorated MoS_2 were deposited on quantifoil Cu grids (300-mech holey carbon). The TEM experiments were performed by JEM-2100F. Raman scattering was performed on a Raman spectrometer with excitation by 640 nm laser light. XPS was carried out at 4D beamlines at Research Institute of Advanced Materials (RIAM).

4.2.4. Sensor measurements

The gas-sensing measurements were performed in a quartz tube with an external heat source. The gas-sensing properties of noble metal decorated MoS_2 sensors were measured at 150 °C. As the flow gas was changed from dry air to a calibrated test gas (balanced with dry air, Sinjin Gases), the variation in the sensor resistance was monitored using a source measurement unit (Kithley 2400). A constant flow rate of 1000 sccm was used for dry air and the test gas. The sensor resistance was measured DC bias voltage of 0.5V. The response of the sensors ($\Delta R/R_0$*100) was accurately determined by measuring the baseline resistances of the sensors in dry air and the saturated resistances after exposure to the test gas. Gas flow was controlled using mass flow controllers, and all the measurements were recorded using a computer over a GPIB interface.

4.3. Result and discussion

4.3.1. Fabrication process of metal decorated MoS_2

The schematic in Figure 4.1 illustrates the fabrication process of the controlled process of decorating Au, Pd and Pt nanoparticled onto MoS_2 and forming the resulting film for gas sensing devices. First, ultrafine MoS_2 powder (Graphene supermarket, average particle size < 90nm, 99%) was exfoliated in an ethanol/water mixture. Aqueous solutions of gold chloride monohydrate ($HAuCl_4 \cdot H_2O$), potassium tetrachloropalladate (K_2PdCl_4), and potassium

tetrachloroplatinate (K_2PtCl_4) was injected into MoS_2 solution at a controlled molar concentration. After simple stirring with heating, high-resolution Au, Pd and Pt nanoparticles were spontaneously decorated onto the MoS_2 layers because of a redox reaction between MoS_2 and noble metal ions. To remove the residual metal salts, each solution is centrifuged with deionized water with 13500 rpm for 10 min. The final solution is dispersed in 1ml of distilled water. After dispersion, each solution was drop-casted onto the interdigitated electrodes (IDEs) for 0.5 µl. To remove DI water after drop-casting, the sensor was annealed on 100 ^oC hotplate for 30 min. The gas sensing properties of fabricated sensor was measured in a quartz tube at 150°C by monitoring the change of the sensor resistance on flowing dry air to a calibrated target gas (Figure4.2).

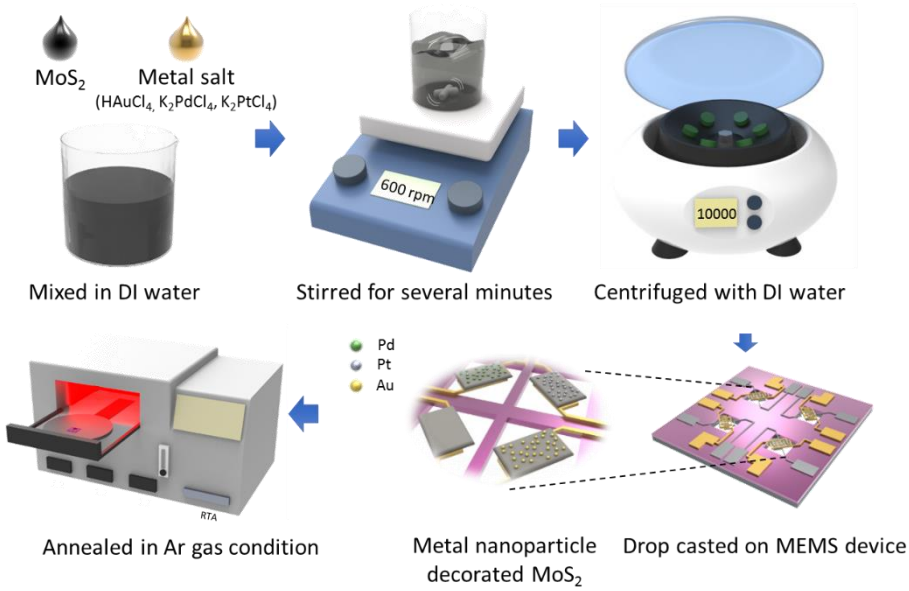

Figure 4.1. Schematic illustration of the fabrication process of noble metal nanoparticle decorated MoS_2

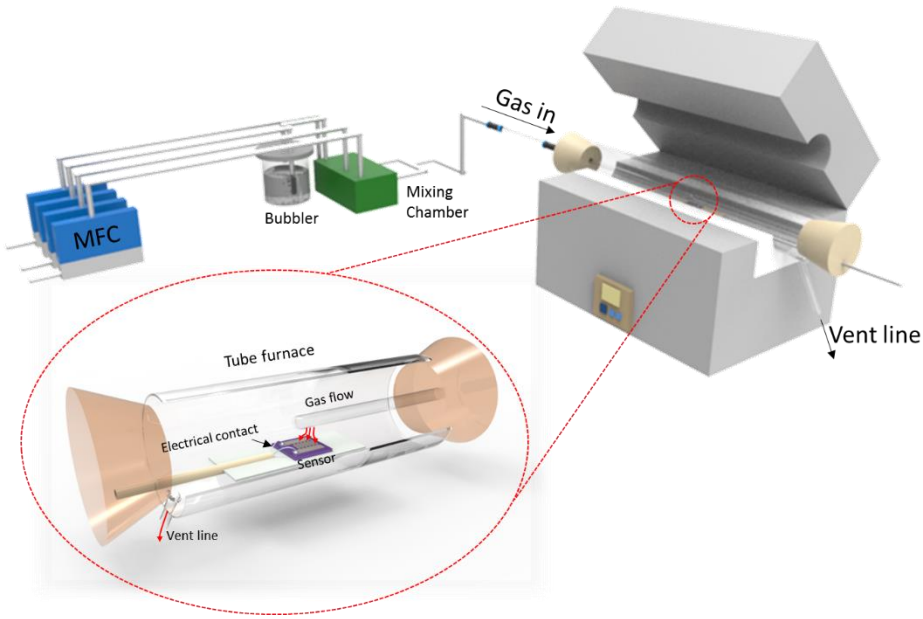

Figure 4.2. Schematic of sensing measurement system.

Since the work function of MoS_2 is 4.55 eV, the Fermi level of MoS_2 is about +0.05V higher than the potential of the standard hydrogen electrode (4.5eV). This is much higher than the reduction potentials of +1.002, +0.591 and +0.755V of $AuCl^{4-}$, $PdCl_4^{2-}$ and $PtCl_4^{2-}$. This potential difference results in spontaneous electron transfer from MoS_2 to metal ions, indicating that metal nanoparticles can form on the MoS_2 through a redox reaction between MoS_2 and the metal salt (Figure 4.3). In particular, the dangling bond and edge sites of partially unbound sulfur MoS_2 are expected to be the main sites for seeding of the metal nucleus.[131,132]

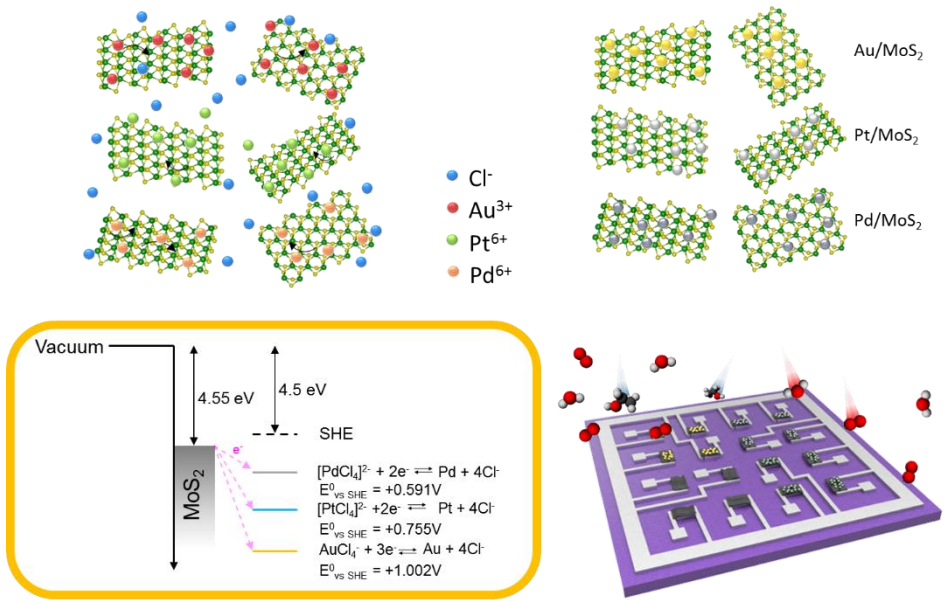

Figure 4.3. Energy diagram showing the work function of MoS_2 and the Pd^{2+}/Pd^0, Au^{3+}/Au^0, Pt^{2+}/Pt^0 reduction potential (1.002V vs. SHE)

4.3.2. Characterization of metal decorated MoS_2

The approximate morphology of the metal nanoparticles decorated on the surface of MoS_2 is shown in the SEM images (Figure 4.4). TEM analysis was performed for more accurate analysis. As a result, the interlayer distance was found to be 0.27 nm, confirming that it was MoS_2 (Figure 4.5a). In addition, the TEM images shown in Figure 4.5d, e and f show that Au nanoparticles are 5 nm, Pd nanoparticles are 10 nm, and Pt nanoparticles are about 5 nm in size. The insets in each Figure 4.5a, b, c, and d show that all of them had an FCC crystal structures. The EDS analysis shown in Figure4.6 confirmed that Pd, Au and Pt nanoparticles were well synthesized on the surface of MoS_2.

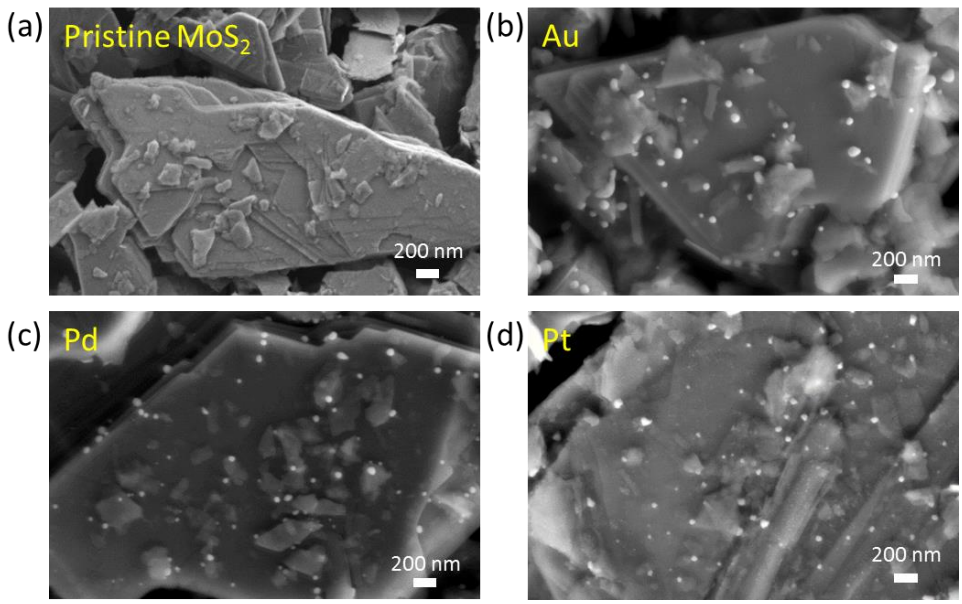

Figure 4.4. SEM images of (a) pristine MoS_2, (b) Au-MoS_2, (c) Pd-MoS_2 and (d) Pt-MoS_2

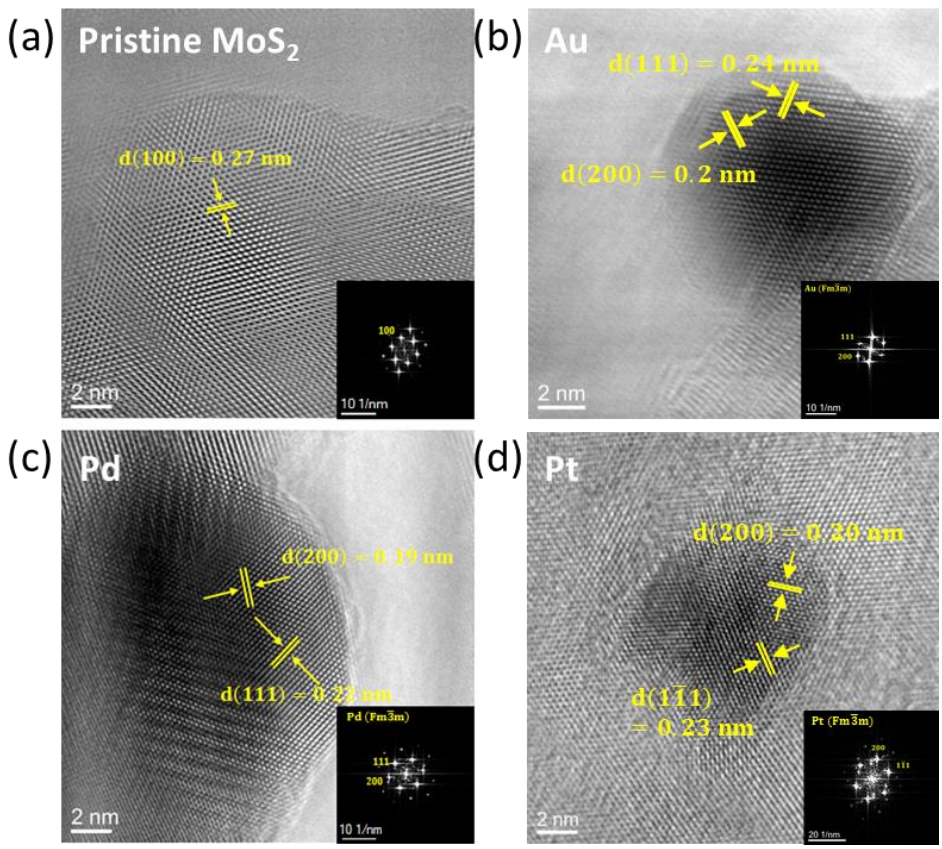

Figure 4.5. HRTEM images of (a) pristine MoS_2, (b) Au-MoS_2, (c) Pd-MoS_2 and (d) Pt-MoS_2.

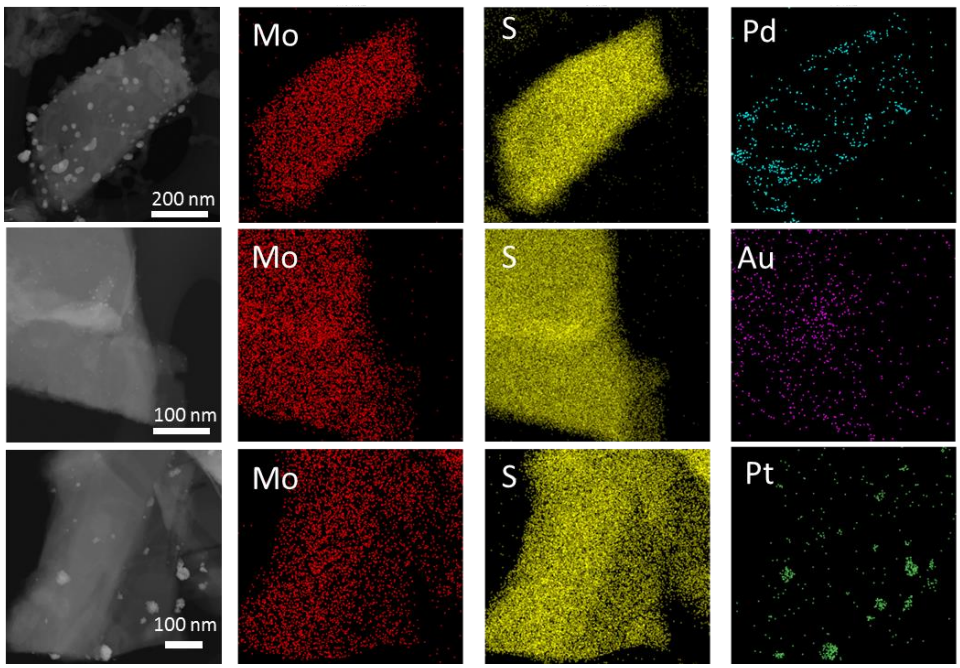

Figure 4.6. TEM EDS of MoS_2 with Au, Pd and Pt nanoparticles.

In order to determine the effects of the Au, Pd, and Pt-doping of MoS_2, Raman spectroscopy, and X-ray photoelectron spectroscopy (XPS) were performed. Raman spectra show that pristine MoS_2 produces two representative vibration peaks, E^1_{2g} and A_{1g}, at 380 and 406 cm^{-1} respectively (Figure 4.7a). The E^1_{2g} phonon mode represents in-plane vibrations of Mo and S atoms, whereas the A_{1g} peak represents the out-of-plane vibration of S atoms. Upon decoration of pristine MoS_2 with Au, Pd and Pt nanoparticles, the E^1_{2g} peak downshifted to 378, 376, and 378 cm^{-1}. The A_{1g} peaks of Au, Pd and Pt nanoparticles also showed downshift to 404, 403 and 404 cm^{-1} individually, suggesting MoS_2 were *n*-type doped by Au, Pd, and Pt nanoparticles.

XPS results further confirm the presence of n-doping upon decoration. Figure 4.7b-f show XPS core level spectra of Mo 3d and S 2p for pristine MoS_2, Au-decorated MoS_2, Pd-decorated MoS_2 and Pt-decorated MoS_2. The peaks for Mo $3d_{3/2}$ and Mo $3d_{5/2}$ of pristine MoS_2 are located at binding energies around 231.87 and 228.67 eV, as well as for the S 2p peaks, which are located at around 167.77 and 161.57 eV. The former peaks are attributed to the Mo $3d_{5/2}$ and Mo $3d_{3/2}$ orbitals of Mo^{4+}, and the latter are due to the S $2p_{1/2}$ and S $2p_{3/2}$ orbitals of the divalent sulfide ions (S^{2-}) in MoS_2. Compared to the peaks of pristine MoS_2, peaks for Mo $3d_{3/2}$, Mo$3d_{5/2}$, S $2s_{1/2}$, and S $2s_{3/2}$ are shifted slightly to higher binding energy after Au (Mo $3d_{3/2}$ = 232.09 eV, Mo $3d_{5/2}$ = 228.99 eV, S $2s_{1/2}$ = 162.99 eV,

and S $2d_{3/2}$ = 162.79 eV), Pd (Mo $3d_{3/2}$ = 232.13 eV, Mo $3d_{5/2}$ = 229.03 eV, S $2s_{1/2}$ = 163.06 eV, and S $2d_{3/2}$ = 161.83 eV), and Pt (Mo $3d_{3/2}$ = 232.54 eV, Mo $3d_{5/2}$ = 229.34 eV, S $2s_{1/2}$ = 163.44 eV, and S $2d_{3/2}$ = 162.24 eV) decoration due to the electronic interaction between Au, Pd, and Pt with the interface of MoS_2. Figure 4.7d–f provides the binding energies of three different noble metals on the surface of MoS_2. Peaks located at about 87.2 eV and 83.6 eV can be ascribed to Au $4f_{5/2}$ and Au $4f_{7/2}$, respectively; peaks representing Pd $3d_{3/2}$ and Pd $3d_{5/2}$ are near 340.5 eV and 335.2 eV, respectively; peaks at 74.6 eV and 71.3 eV originate from Pt $4f_{5/2}$ and Pt $4f_{7/2}$, confirming the decoration of MoS_2 with Au, Pd and Pt nanoparticles[133]. XPS peaks indicate the successful deposition of different noble metals onto the surface of the surface of MoS_2. According to the blue-shift to higher binding energies compared to that of pristine MoS_2, indicating an up-shift to the Fermi level in MoS_2 due to n-type doping. Raman spectroscopy and XPS confirmed that charge transfer from Au, Pd, and Pt nanoparticles to MoS_2 induces n-doping effects on the MoS_2.

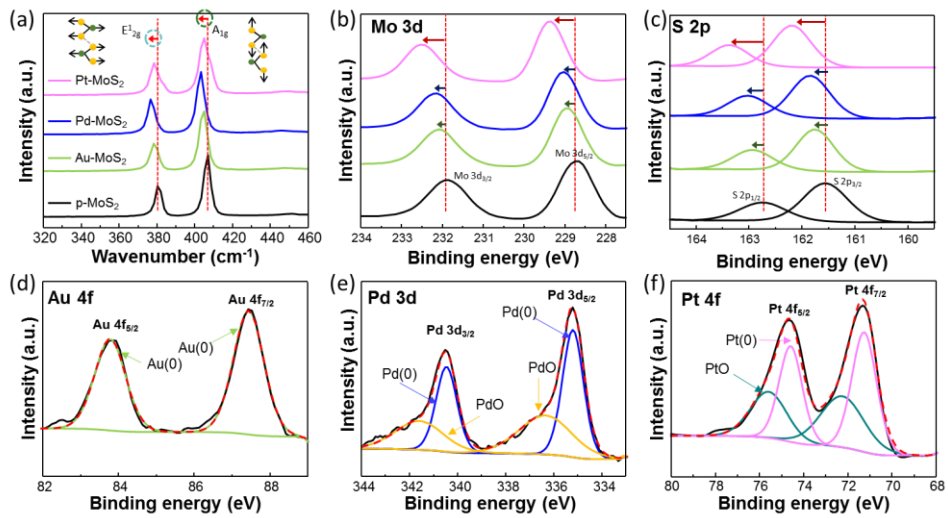

Figure 4.7. Characterization of pristine MoS_2, Au-MoS_2, Pd-MoS_2 and Pt-MoS_2 with (a) Raman spectroscopy and (b-c) XPS. The main peaks of MoS_2 is shown with (b) Mo 3d and (c) S 2p. XPS analysis of (d) Au, (e) Pd, and (f) Pt nanoparticles.

4.3.3. Gas sensing properties

The experimental results indicate that the metal nanoparticle decorated on the MoS_2 strongly affects the gas sensing properties. Figure 4.8 show the dynamic sensing transients of the metal nanoparticle decorated MoS_2. The device was exposed to four consecutive pulses of 50 ppm of NH_3, 50 ppm of H_2, 50 ppm of C_2H_5OH, 50 ppm of CH_3COCH_3, 5 ppm of NO_2, and 5 ppm of H_2S gases. The sensing properties of MoS_2 were 63.46, 40.02, 77.325, 23.05, 651.53 and 46.64% to CH_3COCH_3, C_2H_5OH, H_2, H_2S, NH_3 and NO_2 gases (Figure 4.8a). Au-decorated MoS_2 showed 29.35, 165.28, 36.86, 32.71, 80.37 and 87.0 % response to each gas (Figure 4.8b). The response of Pd-decorated MoS_2 was 58.32, 102.62, 1027.1, 113.79, 371.69, and 26.92% (Figure 4.8c). Pt-decorated MoS_2 showed 89.48, 101.41, 256.5, 27.8, 366.71, and 77.38% response to six gases (Figure 4.8d).

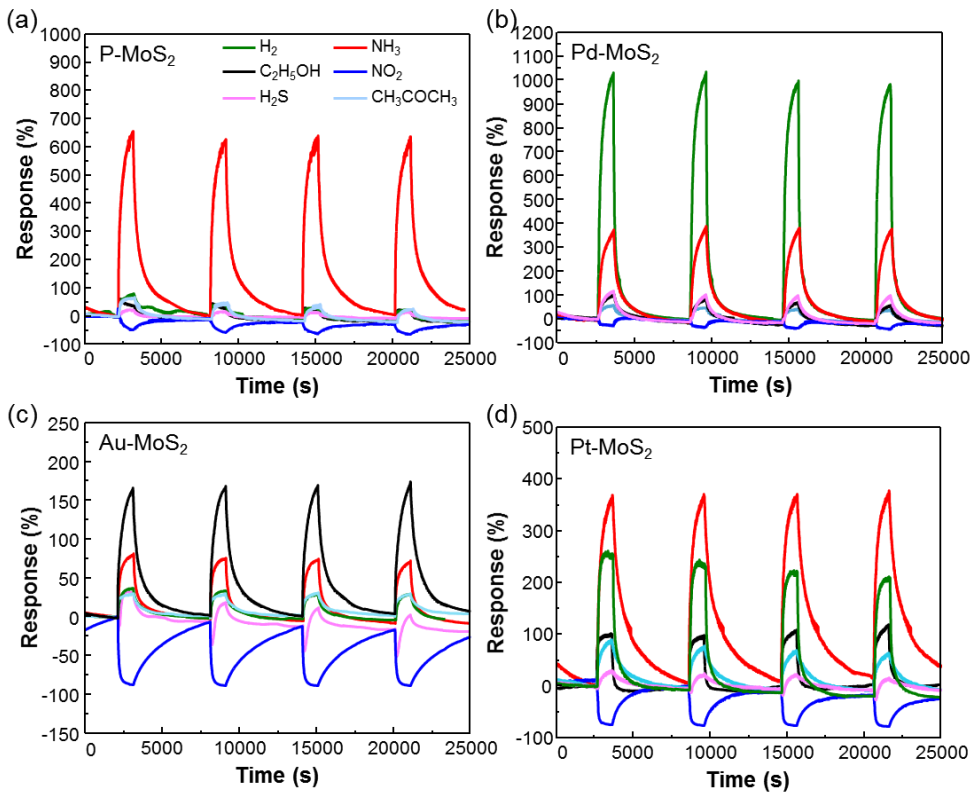

Figure 4.8. The response curves of (a) p-MoS_2, (b) Au-MoS_2, (c) Pd-MoS_2 and (d) Pt-MoS_2 to 50 ppm H_2, 50 ppm NH_3, 50 ppm C_2H_5OH, 50 ppm CH_3COCH_3, 5 ppm NO_2 and 5 ppm H_2S at 150 ^oC.

Figure 4.9 show radar charts of gas sensitivity toward CH_3COCH_3, C_2H_5OH, H_2, H_2S, NH_3 and NO_2 gas species. The pristine MoS_2 and Pd-decorated MoS_2 sensor showed high sensitivity toward NH_3 and H_2 gas respectively. Au-decorated MoS_2 sensor showed superior sensitivity to ethanol gas. Pt-decorated MoS_2 sensor was highly sensitive to H_2 and NH_3 gases.

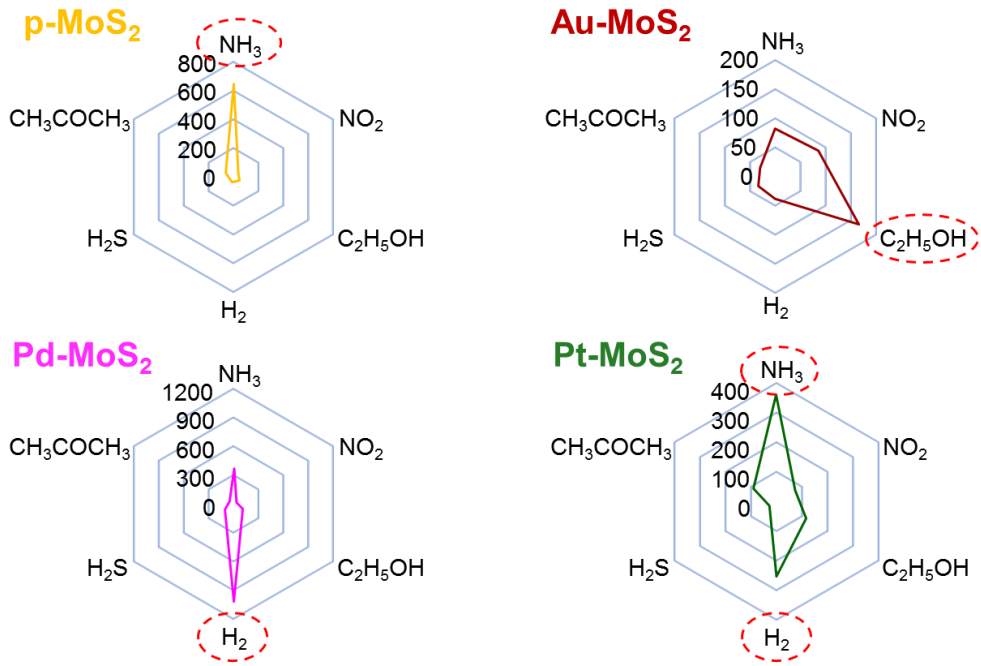

Figure 4.9. Polar plot of response of p-MoS_2, Pd-MoS_2, Au-MoS_2 and Pt-MoS_2.

4.4. Conclusion

In conclusion, we have reported high sensitivity of noble metal decorated MoS_2 gas sensor array prepared facile fabrication steps. The surface of MoS_2 was decorated with well dispersed Gold, Palladium and Silver nanoparticles using solution process. All sensors were exposed to 5 ppm of NO_2, 50 ppm NH_3, 50 ppm H_2, 50 ppm CH_3COCH_3 and 50 ppm C_2H_5OH gas. Each sensor showed enhanced selectivity to different gases. Pristine MoS_2 showed high sensitivity to NH_3 gas. Compared to this result, Au-decorated MoS_2 showed selectivity to NO_2 gas. Pd-decorated MoS_2 showed increased sensitivity to H_2 gas and Ag-decorated MoS_2 showed high selectivity to H_2 and H_2S gas. To these excellent properties, it is expected that the significantly simple fabrication process enlarges the potential of noble metal decorated MoS_2 sensor array for practical application in environmental monitoring.

REERENCES

[1] S. Sankaran, L.R. Khot, S. Panigrahi, Biology and applications of olfactory sensing system: A review, *Sens. Actuators, B* **2012**, *171*, 1–17.

[2] A.D. Wilson, M. Baietto, Applications and advances in electronic-nose technologies, *Sensors* **2009**, *9*, 5099–5148.

[3] L. Zhang, F. Tian, H. Nie, L. Dang, G. Li, Q. Ye, C. Kadri, Classification of multiple indoor air contaminants by an electronic nose and a hybrid support vector machine, *Sens. Actuators, B* **2012**, *174*, 114–125.

[4] S. Dragonieri, M.P. Van Der Schee, T. Massaro, N. Schiavulli, P. Brinkman, A. Pinca, P. Carratú, A. Spanevello, O. Resta, M. Musti, P.J. Sterk, An electronic nose distinguishes exhaled breath of patients with Malignant Pleural Mesothelioma from controls, *Lung Cancer.* **2012,** *75* 326–331.

[5] D. Guo, D. Zhang, N. Li, L. Zhang, J. Yang, A novel breath analysis system based on electronic olfaction, *IEEE TRANSACTIONS ON BIOMEDICAL ENGINEERING* 1 **2010,** *57*, 2753–2763.

[6] Z. Haddi, A. Amari, H. Alami, N. El Bari, E. Llobet, B. Bouchikhi, A portable electronic nose system for the identification of cannabis-based drugs, *Sens. Actuators, B* **2011**, *155*, 456–463.

[7] C. Di Natale, A. Macagnano, E. Martinelli, R. Paolesse, E. Proietti, A. D'Amico, The evaluation of quality of post-harvest oranges and apples by means of an electronic nose, *Sens. Actuators, B* **2001**, *78* 26–31.

[8] I. Concina, M. Falasconi, V. Sberveglieri, Electronic noses as flexible tools to assess food quality and safety: Should we trust them?, *IEEE Sens. J.* **2012,** *12*, 3232–3237.

[9] M.M. Macías, A.G. Manso, C.J.G. Orellana, H.M.G. Velasco, R.G. Caballero, J.C.P. Chamizo, Acetic acid detection threshold in synthetic wine samples of a portable electronic nose, *Sensors.* **2013,** *13*, 208–220.

[10] S. Ampuero, J.O. Bosset, The electronic nose applied to dairy products: A review, *Sens. Actuators, B* **2003**, *94*, 1–12.

[11] A. Berna, Metal oxide sensors for electronic noses and their application to food analysis, *Sensors.* **2010,** *10,* 3882–3910.

[12] E.A. Baldwin, J. Bai, A. Plotto, S. Dea, Electronic noses and tongues: Applications for the food and pharmaceutical industries, *Sensors.* **2011,** *11*, 4744–4766.

[13] Najam ul Hasan, N. Ejaz, W. Ejaz, H.S. Kim, Meat and fish freshness inspection system based on odor sensing, *Sensors.* **2012,** *12*, 15542–15557.

[14] J.W. Gardner, H.W. Shin, E.L. Hines, C.S. Dow, Electronic nose system for monitoring the quality of potable water, *Sens. Actuators, B* **2000,** *69*, 336–341.

[15] R.E. Baby, M. Cabezas, E.N. Walsöe De Reca, Electronic nose: A useful tool for monitoring environmental contamination, *Sens. Actuators, B* **2000,** *69*, 214–218.

[16] K. Ho, Clifford, C. Hughes, Robert, In-Situ Chemiresistor sensor package for real-time detection of volatile organic compounds in soil and groundwater, *Sensors.* **2002,** *2*, 23–34.

[17] D. Explosives, Detection of explosives and landmines, **2012**.

[18] A.D. Wilson, Review of electronic-nose technologies and algorithms to detect hazardous chemicals in the environment, *Procedia Technol.* **2012,** *1*, 453–463.

[19] F. Tsow, E. Forzani, A. Rai, R. Wang, N.J. Tao, R. Tsui, S. Mastroianni, C. Knobbe, J. Gandolfi, A wearable and wireless sensor system for real-time monitoring of toxic environmental volatile organic compounds, *IEEE Sens. J.* **2009,** *9*, 1734–1740.

[20] K. Arshak, E. Moore, G.M. Lyons, J. Harris, S. Clifford, A review of gas sensors employed in electronic nose applications, *Sens. Rev.* **2004,** *24,* 181–198.

[21] C. Wang, L. Yin, L. Zhang, D. Xiang, R. Gao, Metal oxide gas sensors: Sensitivity and influencing factors, *Sensors.* **2010,** *10,* 2088–2106.

[22] J.M. Suh, Y.S. Shim, D.H. Kim, W. Sohn, Y. Jung, S.Y. Lee, S. Choi, Y.H. Kim, J.M. Jeon, K. Hong, K.C. Kwon, S.Y. Park, C. Kim, J.H. Lee, C.Y. Kang, H.W. Jang, Synergetically selective toluene sensing in hematite-decorated nickel oxide nanocorals, *Adv. Mater. Technol.* **2017,** *2,* 1–10.

[23] J.M. Suh, W. Sohn, Y.S. Shim, J.S. Choi, Y.G. Song, T.L. Kim, J.M. Jeon, K.C. Kwon, K.S. Choi, C.Y. Kang, H.G. Byun, H.W. Jang, P-p Heterojunction of nickel oxide-decorated cobalt oxide nanorods for enhanced sensitivity and selectivity toward volatile organic compounds, *ACS Appl. Mater. Interfaces.* **2018,** *10,* 1050–1058.

[24] A.A. Tomchenko, G.P. Harmer, B.T. Marquis, J.W. Allen, Semiconducting metal oxide sensor array for the selective detection of combustion gases, *Sens. Actuators, B* **2003,** *93,* 126–134.

[25] D.H. Kim, T.H. Kim, W. Sohn, J.M. Suh, Y.S. Shim, K.C. Kwon, K. Hong, S. Choi, H.G. Byun, J.H. Lee, H.W. Jang, Au decoration of vertical hematite nanotube arrays for further selective detection of acetone in exhaled breath, *Sens. Actuators, B* **2018,** *274,* 587–594.

[26] C.S. Lee, H.Y. Li, B.Y. Kim, Y.M. Jo, H.G. Byun, I.S. Hwang, F. Abdel-Hady, A.A. Wazzan, J.H. Lee, Discriminative detection of indoor volatile organic compounds using a sensor array based on pure and Fe-doped In_2O_3 nanofibers, *Sens. Actuators, B* **2019,** *285* 193–200.

[27] T.H. Kim, A. Hasani, L. Van Quyet, Y. Kim, S.Y. Park, M.G. Lee, W. Sohn, T.P. Nguyen, K.S. Choi, S.Y. Kim, H.W. Jang, NO_2 sensing properties of

porous Au-incorporated tungsten oxide thin films prepared by solution process, *Sens. Actuators, B* **2019,** *286* 512–520.

[28] Y.H. Kim, K.Y. Kim, Y.R. Choi, Y.S. Shim, J.M. Jeon, J.H. Lee, S.Y. Kim, S. Han, H.W. Jang, Ultrasensitive reversible oxygen sensing by using liquid-exfoliated MoS_2 nanoparticles, *J. Mater. Chem. A.* **2016,** *4*, 6070–6076.

[29] Y.S. Shim, K.C. Kwon, J.M. Suh, K.S. Choi, Y.G. Song, W. Sohn, S. Choi, K. Hong, J.M. Jeon, S.P. Hong, S. Kim, S.Y. Kim, C.Y. Kang, H.W. Jang, Synthesis of numerous edge sites in MoS_2 via SiO_2 nanorods platform for highly sensitive gas sensor, *ACS Appl. Mater. Interfaces.* **2018,** *10*, 31594–31602.

[30] S. Varghese, S. Varghese, S. Swaminathan, K. Singh, V. Mittal, Two-dimensional materials for sensing: Graphene and beyond, *Electronics.* **2015,** *4*, 651–687.

[31] Y.H. Kim, J.S. Park, Y.R. Choi, S.Y. Park, S.Y. Lee, W. Sohn, Y.S. Shim, J.H. Lee, C.R. Park, Y.S. Choi, B.H. Hong, J.H. Lee, W.H. Lee, D. Lee, H.W. Jang, Chemically fluorinated graphene oxide for room temperature ammonia detection at ppb levels, *J. Mater. Chem. A.* **2017**, *5*, 19116–19125.

[32] T. A.P.F., M. N., Electronic noses and disease diagnostics, *Nat. Rev. Microbiol.* **2004,** *2*, 160–166.

[33] N. Barsan, D. Koziej, U. Weimar, Metal oxide-based gas sensor research: How to?, *Sens. Actuators, B* **2007,** *121*, 18–35.

[34] S. Choopun, N. Hongsith, E. Wongrat, Metal-oxide nanowires for gas sensors, Nanowires - Recent Adv. (2012) 3–24.

[35] J. Li, Y. Lu, Q. Ye, M. Cinke, J. Han, M. Meyyappan, Carbon nanotube sensors for gas and organic vapor detection, *Nano Lett.* **2003,** *3*, 929–933.

[36] F. Schedin, A.K. Geim, S. V. Morozov, E.W. Hill, P. Blake, M.I. Katsnelson, K.S. Novoselov, Detection of individual gas molecules adsorbed on graphene, *Nat. Mater.* **2007,** *6,* 652–655.

[37] A. Lipatov, A. Varezhnikov, P. Wilson, V. Sysoev, A. Kolmakov, A. Sinitskii, Highly selective gas sensor arrays based on a thermally reduced graphene oxide, *Nanoscale,* **2013,** *5,* 5426–5434.

[38] M. M. Pour, A. Lashkov, A. Radocea, X. Liu, T. Sun, A. Lipatov, R. A. Korlacki, M. Shekhirev, N. R. Aluru, J. W. Lyding, V. Sysoev, A. Sinitskii, Laterally extended atomatically precise garphene nanoribbons with improved electrical conductivity for efficient gas sensing, *Nat. Comm.* **2017,** *8,* 820.

[39] Y. Dan, Y. Lu, N.J. Kybert, Z. Luo, A.T.C. Johnson, Intrinsic response of graphene vapor sensors, *Nano Lett.* **2009,** *9,* 1472–1475.

[40] J.T. Robinson, F.K. Perkins, E.S. Snow, Z. Wei, P.E. Sheehan, Reduced graphene oxide molecular sensors, *Nano Lett.* **2008,** *8,* 3137–3140.

[41] G. Lu, L.E. Ocola, J. Chen, Gas detection using low-temperature reduced graphene oxide sheets, *Appl. Phys. Lett.* **2009,** *94,* 2–5.

[42] A. Lipatov, A. Varezhnikov, P. Wilson, V. Sysoev, A. Kolmakov, A. Sinitskii, Highly selective gas sensor arrays based on thermally reduced graphene oxide, *Nanoscale.* **2013,** *5,* 5426–5434.

[43] S. Cui, H. Pu, E.C. Mattson, Z. Wen, J. Chang, Y. Hou, C.J. Hirschmugl, J. Chen, Ultrasensitive chemical sensing through facile tuning defects and functional groups in reduced graphene oxide, *Anal. Chem.* **2014,** *86,* 7516–7522.

[44] J.Z. Ou, W. Ge, B. Carey, T. Daeneke, A. Rotbart, W. Shan, Y. Wang, Z. Fu, A.F. Chrimes, W. Wlodarski, S.P. Russo, Y.X. Li, K. Kalantar-Zadeh,

Physisorption-based charge transfer in two-dimensional SnS_2 for selective and reversible NO_2 gas sensing, *ACS Nano.* **2015,** *9,* 10313–10323.

[45] K. Y. Ko, J. -G. Song, Y. Kim, T. Kim, T. Choi, S. Shin, C. W. Lee, K. Lee, J. Koo, H. Lee, J. Kim, T. Lee, J. Park, H. Kim, Improvement of gas-sensing performance of large-area tungsten disulfide nanosheets by surface functionalization, *ACS Nano.* **2016,** *10,* 9287-8296.

[46] D.J. Late, Y.K. Huang, B. Liu, J. Acharya, S.N. Shirodkar, J. Luo, A. Yan, D. Charles, U. V. Waghmare, V.P. Dravid, C.N.R. Rao, Sensing behavior of atomically thin-layered MoS_2 transistors, *ACS Nano.* **2013,** *7,* 4879–4891.

[47] Y.I. Jhon, Y. Kim, J. Park, J.H. Kim, T. Lee, M. Seo, Y.M. Jhon, Significant exciton brightening in monolayer tungsten disulfides via fluorination: n-type gas sensing semiconductors, *Adv. Funct. Mater.* **2016,** *26,* 7551–7559.

[48] S.Y. Cho, S.J. Kim, Y. Lee, J.S. Kim, W. Bin Jung, H.W. Yoo, J. Kim, H.T. Jung, Highly enhanced gas adsorption properties in vertically aligned MoS_2 layers, *ACS Nano.* **2015,** *9,* 9314–9321.

[49] S.Y. Cho, Y. Lee, H.J. Koh, H. Jung, J.S. Kim, H.W. Yoo, J. Kim, H.T. Jung, Superior chemical sensing performance of black phosphorus: comparison with MoS_2 and Graphene, *Adv. Mater.* **2016,** *28,* 7020–7028.

[50] B. Cho, A.R. Kim, D.J. Kim, H.S. Chung, S.Y. Choi, J.D. Kwon, S.W. Park, Y. Kim, B.H. Lee, K.H. Lee, D.H. Kim, J. Nam, M.G. Hahm, Two-dimensional atomic-layered alloy junctions for high-performance wearable chemical sensor, *ACS Appl. Mater. Interfaces.* **2016,** *8,* 19635–19642.

[51] B. Cho, M.G. Hahm, M. Choi, J. Yoon, A.R. Kim, Y.J. Lee, S.G. Park, J.D. Kwon, C.S. Kim, M. Song, Y. Jeong, K.S. Nam, S. Lee, T.J. Yoo, C.G. Kang, B.H. Lee, H.C. Ko, P.M. Ajayan, D.H. Kim, Charge-transfer-based gas sensing using atomic-layer MoS_2, *Sci. Rep.* **2015,** *5,* 8052.

[52] M. Swan, Sensor mania! the internet of things, wearable computing, objective metrics, and the quantified self 2.0, *J. Sens. Actuator Networks.* **2012,** *1*, 217–253.

[53] A.C. Lowen, S. Mubareka, J. Steel, P. Palese, Influenza virus transmission is dependent on relative humidity and temperature, *PLoS Pathog.* **2007,** *3*, 1470–1476.

[54] H. Farahani, R. Wagiran, M.N. Hamidon, Humidity sensors principle, mechanism, and fabrication technologies: A comprehensive review, **2014**.

[55] Z. Chen, C. Lu, Humidity sensors: A review of materials and mechanisms, *Sens. Lett.* **2005,** *3*, 274–295.

[56] P.G. Su, C.S. Wang, Novel flexible resistive-type humidity sensor, *Sens. Actuators, B* **2007,** *123*, 1071–1076.

[57] P.M. Harrey, B.J. Ramsey, P.S.A. Evans, D.J. Harrison, Capacitive-type humidity sensors fabricated using the offset lithographic printing process, *Sens. Actuators, B* **2002,** *87*, 226–232.

[58] J. Lee, S. Mulmi, V. Thangadurai, S.S. Park, Magnetically aligned Iron Oxide/Gold nanoparticle-decorated carbon nanotube hybrid structure as a humidity sensor, *ACS Appl. Mater. Interfaces.* **2015,** *7* 15506–15513.

[59] R.S. Jachowicz, S.D. Senturia, A thin-film capacitance humidity sensor, *Sensors and Actuators.* **1981,** *2*, 171–186.

[60] F.L. Meng, Z. Guo, X.J. Huang, Graphene-based hybrids for chemiresistive gas sensors, *TrAC - Trends Anal. Chem.* **2015,** *68*, 37–47.

[61] D. Burman, R. Ghosh, S. Santra, P.K. Guha, Highly proton conducting MoS_2/graphene oxide nanocomposite based chemoresistive humidity sensor, *RSC Adv.* **2016,** *6*, 57424–57433.

[62] D.I. Lim, J.R. Cha, M.S. Gong, Preparation of flexible resistive micro-humidity sensors and their humidity-sensing properties, *Sens. Actuators, B* **2013,** *183,* 574–582.

[63] A.D. Smith, K. Elgammal, F. Niklaus, A. Delin, A.C. Fischer, S. Vaziri, F. Forsberg, M. Råsander, H. Hugosson, L. Bergqvist, S. Schröder, S. Kataria, M. Östling, M.C. Lemme, Resistive graphene humidity sensors with rapid and direct electrical readout, *Nanoscale.* **2015,** *7,* 19099–19109.

[64] D.H. Kim, Y.S. Shim, J.M. Jeon, H.Y. Jeong, S.S. Park, Y.W. Kim, J.S. Kim, J.H. Lee, H.W. Jang, Vertically ordered hematite nanotube array as an ultrasensitive and rapid response acetone sensor, *ACS Appl. Mater. Interfaces.* **2014,** *6,* 14779–14784.

[65] M.M. Arafat, B. Dinan, S.A. Akbar, A.S.M.A. Haseeb, Gas sensors based on one dimensional nanostructured metal-oxides: A review, *Sensors.* **2012,** *12,* 7207–7258.

[66] Y. Sakai, Y. Sadaoka, M. Matsuguchi, Humidity sensors based on polymer thin films, *Sens. Actuators, B* **1996,** *35,* 85–90.

[67] X. Wang, B. Ding, J. Yu, M. Wang, Highly sensitive humidity sensors based on electro-spinning/netting a polyamide 6 nano-fiber/net modified by polyethyleneimine, *J. Mater. Chem.* **2011,** *21,* 16231–16238.

[68] W. Yuan, G. Shi, Graphene-based gas sensors, *J. Mater. Chem. A.* **2013,** *1,* 10078–10091.

[69] Y.R. Choi, Y.G. Yoon, K.S. Choi, J.H. Kang, Y.S. Shim, Y.H. Kim, H.J. Chang, J.H. Lee, C.R. Park, S.Y. Kim, H.W. Jang, Role of oxygen functional groups in graphene oxide for reversible room-temperature NO_2 sensing, *Carbon.* **2015,** *9*1, 178–187.

[70] A.K. Geim, K.S. Novoselov, The rise of graphene, *Nat. Mater.* **2007,** *6,* 183–191.

[71] G. Lu, L.E. Ocola, J. Chen, Reduced graphene oxide for room-temperature gas sensors, *Nanotechnology.* **2009,** *20,* 445502.

[72] D.R. Dreyer, S. Park, C.W. Bielawski, R.S. Ruoff, The chemistry of graphene oxide, *Chem. Soc. Rev.* **2010,** *39,* 228–240.

[73] S. Borini, R. White, D. Wei, M. Astley, S. Haque, E. Spigone, N. Harris, J. Kivioja, T. Ryhänen, Ultrafast graphene oxide humidity sensors, *ACS Nano.* **2013,** *7,* 11166–11173.

[74] G. Naik, S. Krishnaswamy, Room-temperature humidity sensing using graphene oxide thin films, *Graphene.* **2016,** *05,* 1–13.

[75] S. Pei, H.M. Cheng, The reduction of graphene oxide, *Carbon.* **2012,** *50,* 3210–3228.

[76] B. Cho, J. Yoon, S.K. Lim, A.R. Kim, D.H. Kim, S.G. Park, J.D. Kwon, Y.J. Lee, K.H. Lee, B.H. Lee, H.C. Ko, M.G. Hahm, Chemical sensing of 2D Graphene/MoS_2 heterostructure device, *ACS Appl. Mater. Interfaces.* **2015,** *7,* 16775–16780.

[77] Z. Guo, F. Du, Z. Cui, Synthesis and characterization of bundle-like structures consisting of single crystal $Ce(OH)CO_3$ nanorods, *Mater. Lett.* **2007,** *61,* 694–696.

[78] C.H. Lu, H.C. Wang, Formation and microstructural variation of cerium carbonate hydroxide prepared by the hydrothermal process, *Mater. Sci. Eng. B Solid-State Mater. Adv. Technol.* **2002,** *90,* 138–141.

[79] K.S. Novoselov, A. Mishchenko, A. Carvalho, A.H. Castro Neto, 2D materials and van der Waals heterostructures, *Science* **2016,** *(80-.).* 353.

[80] X. Li, B. Wang, X. Wang, X. Zhou, Z. Chen, C. He, Z. Yu, Y. Wu, Enhanced NH_3-sensitivity of reduced graphene oxide modified by Tetra-α-Iso-Pentyloxymetallophthalocyanine derivatives, *Nanoscale Res. Lett.* **2015,** *10*.

[81] J. Meng, H.D. Song, C.Z. Li, Y. Jin, L. Tang, D. Liu, Z.M. Liao, F. Xiu, D.P. Yu, Lateral graphene p-n junctions formed by the graphene/MoS_2 hybrid interface, *Nanoscale.* **2015,** *7,* 11611–11619.

[82] H. Wang, J.T. Robinson, X. Li, H. Dai, Solvothermal reduction of chemically exfoliated graphene sheets, *J. Am. Chem. Soc.* **2009,** *131,* 9910–9911.

[83] Y. Li, H. Wang, L. Xie, Y. Liang, G. Hong, H. Dai, MoS_2 nanoparticles grown on graphene: An advanced catalyst for the hydrogen evolution reaction, *J. Am. Chem. Soc.* **2011,** *133,* 7296–7299.

[84] H. Li, K. Yu, C. Li, Z. Tang, B. Guo, X. Lei, H. Fu, Z. Zhu, Charge-transfer induced high efficient hydrogen evolution of MoS_2/graphene cocatalyst, *Sci. Rep.* **2015,** *5,* 1–11.

[85] Y.H. Kim, S.J. Kim, Y.J. Kim, Y.S. Shim, S.Y. Kim, B.H. Hong, H.W. Jang, Self-activated transparent all-graphene gas sensor with endurance to humidity and mechanical bending, *ACS Nano.* **2015,** *9,* 10453–10460.

[86] S. Stankovich, D.A. Dikin, R.D. Piner, K.A. Kohlhaas, A. Kleinhammes, Y. Jia, Y. Wu, S.B.T. Nguyen, R.S. Ruoff, Synthesis of graphene-based nanosheets via chemical reduction of exfoliated graphite oxide, *Carbon.* **2007,** *45,* 1558–1565.

[87] D.B. Nimbalkar, H.H. Lo, P.V.R.K. Ramacharyulu, S.C. Ke, Improved photocatalytic activity of RGO/MoS_2 nanosheets decorated on TiO_2 nanoparticles, *RSC Adv.* **2016,** *6,* 31661–31667.

[88] A. Ghosh, D.J. Late, L.S. Panchakarla, A. Govindaraj, C.N.R. Rao, NO_2 and humidity sensing characteristics of few-layer graphenes, *J. Exp. Nanosci.* **2009,** *4,* 313–322.

[89] H. Li, Q. Zhang, C.C.R. Yap, B.K. Tay, T.H.T. Edwin, A. Olivier, D. Baillargeat, From bulk to monolayer MoS_2: Evolution of Raman scattering, *Adv. Funct. Mater.* **2012,** *22,* 1385–1390.

[90] J.M. Jeon, Y.S. Shim, S.D. Han, D.H. Kim, Y.H. Kim, C.Y. Kang, J.S. Kim, M. Kim, H.W. Jang, Vertically ordered SnO_2 nanobamboos for substantially improved detection of volatile reducing gases, *J. Mater. Chem. A.* **2015,** *3,* 17939–17945.

[91] H. Zhang, Y.N. Zhang, H. Liu, L.M. Liu, Novel heterostructures by stacking layered molybdenum disulfides and nitrides for solar energy conversion, *J. Mater. Chem. A.* **2014,** *2,* 15389–15395.

[92] H. Wang, D. Tran, J. Qian, F. Ding, D. Losic, MoS_2/Graphene composites as promising materials for energy storage and conversion applications, *Adv. Mater. Interfaces.* **2019,** *6,* 1–23.

[93] D.P. Kumar, S. Hong, D.A. Reddy, T.K. Kim, Ultrathin MoS_2 layers anchored exfoliated reduced graphene oxide nanosheet hybrid as a highly efficient cocatalyst for CdS nanorods towards enhanced photocatalytic hydrogen production, *Appl. Catal. B Environ.* **2017,** *212,* 7–14.

[94] M.A. Bissett, I.A. Kinloch, R.A.W. Dryfe, Characterization of MoS_2-Graphene composites for high-performance coin cell supercapacitors, *ACS Appl. Mater. Interfaces.* **2015,** *7,* 17388–17398.

[95] N. Savjani, E.A. Lewis, M.A. Bissett, J.R. Brent, R.A.W. Dryfe, S.J. Haigh, P. O'Brien, Synthesis of lateral size-controlled monolayer 1H-MoS_2@Oleylamine as supercapacitor electrodes., *Chem. Mater.* **2016,** *28,* 657–664.

[96] J.N. Coleman, M. Lotya, A. O'Neill, S.D. Bergin, P.J. King, U. Khan, K. Young, A. Gaucher, S. De, R.J. Smith, I. V. Shvets, S.K. Arora, G. Stanton, H.Y. Kim, K. Lee, G.T. Kim, G.S. Duesberg, T. Hallam, J.J. Boland, J.J.

Wang, J.F. Donegan, J.C. Grunlan, G. Moriarty, A. Shmeliov, R.J. Nicholls, J.M. Perkins, E.M. Grieveson, K. Theuwissen, D.W. McComb, P.D. Nellist, V. Nicolosi, Two-dimensional nanosheets produced by liquid exfoliation of layered materials, *Science* **2011,** *331,* 568–571.

[97] F. Meng, J. Li, S.K. Cushing, M. Zhi, N. Wu, Solar hydrogen generation by nanoscale p-n junction of p-type molybdenum disulfide/n-type nitrogen-doped reduced graphene oxide, *J. Am. Chem. Soc.* **2013,** *135,* 10286–10289.

[98] J. Li, Y. Lu, Q. Ye, M. Cinke, J. Han, M. Meyyappan, Carbon nanotube sensors for gas and organic vapor detection, *Nano Lett.* **2003,** *3,* 929–933.

[99] V. Dua, S.P. Surwade, S. Ammu, S.R. Agnihotra, S. Jain, K.E. Roberts, S. Park, R.S. Ruoff, S.K. Manohar, All-organic vapor sensor using inkjet-printed reduced graphene oxide, *Angew. Chemie - Int. Ed.* **2010,** *49,* 2154–2157.

[100] B. Gupta, N. Kumar, K. Panda, V. Kanan, S. Joshi, I. Visoly-Fisher, Role of oxygen functional groups in reduced graphene oxide for lubrication, *Sci. Rep.* **2017,** *7,* 1–14.

[101] Y. Zhan, Z. Liu, S. Najmaei, P.M. Ajayan, J. Lou, Large-area vapor-phase growth and characterization of MoS_2 atomic layers on a SiO_2 substrate, *Small.* **2012,** *8,* 966–971.

[102] M.L. Tsai, S.H. Su, J.K. Chang, D.S. Tsai, C.H. Chen, C.I. Wu, L.J. Li, L.J. Chen, J.H. He, Monolayer MoS_2 heterojunction solar cells, *ACS Nano.* **2014,** *8,* 8317–8322.

[103] H. Seo, S. Ahn, J. Kim, Y.A. Lee, K.H. Chung, K.J. Jeon, Multi-resistive reduced graphene oxide diode with reversible surface electrochemical reaction induced carrier control, *Sci. Rep.* **2014,** *4,* 1–7.

[104] Q. Feng, X. Li, J. Wang, Percolation effect of reduced graphene oxide (rGO) on ammonia sensing of rGO-SnO_2composite based sensor, *Sens. Actuators, B* **2017,** *243*, 1115–1126.

[105] K. Saetia, J.M. Schnorr, M.M. Mannarino, S.Y. Kim, G.C. Rutledge, T.M. Swager, P.T. Hammond, Spray-layer-by-layer carbon nanotube/electrospun fiber electrodes for flexible chemiresistive sensor applications, *Adv. Funct. Mater.* **2014,** *24*, 492–502.

[106] J.E. Lee, J. Jung, T.Y. Ko, S. Kim, S. Il Kim, J. Nah, S. Ryu, K.T. Nam, M.H. Lee, Catalytic synergy effect of MoS_2/reduced graphene oxide hybrids for a highly efficient hydrogen evolution reaction, *RSC Adv.* **2017,** *7*, 5480–5487.

[107] D. Marx, M.E. Tuckerman, J. Hutter, M. Parrinello, The nature of the hydrated excess proton in water, *Nature.* **1999,** *397*, 601–604.

[108] N. Yamazoe, Y. Shimizu, Humidity sensors: Principles and applications, *Sens, Actuators.* **1986,** *10*, 379–398.

[109] N. Agmon, The Grotthuss mechanism, *Chem. Phys. Lett.* **1995,** *244*, 456–462.

[110] D. Zhang, J. Tong, B. Xia, Humidity-sensing properties of chemically reduced graphene oxide/polymer nanocomposite film sensor based on layer-by-layer nano self-assembly, *Sens. Actuators, B* **2014,** *197*, 66–72.

[111] M.C. Chen, C.L. Hsu, T.J. Hsueh, Fabrication of humidity sensor based on bilayer graphene, *IEEE Electron Device Lett.* **2014,** *35*, 590–592.

[112] A. Lipatov, A. Varezhnikov, P. Wilson, V. Sysoev, A. Kolmakov, A. Sinitskii, Highly selective gas sensor arrays based on thermally reduced graphene oxide, *Nanoscale.* **2013,** *5*, 5426–5434.

[113] H. Bi, K. Yin, X. Xie, J. Ji, S. Wan, L. Sun, M. Terrones, M.S. Dresselhaus, Ultrahigh humidity sensitivity of graphene oxide, *Sci. Rep.* **2013,** *3*, 1–7.

[114] F. Röck, N. Barsan, U. Weimar, Electronic nose: Current status and future trends, *Chem. Rev.* **2008,** *108,* 705–725.

[115] J. Albert, Keith, S. Lewis, Nathan, L. Schauer, Caroline, A. Sotzing, Gregory, E. Stitzel, Shannon, P. Vaid, Thomas, R. Walt, David, Cross-reactive chemical sensor arrays, *Chem. Rev.* **2000,** *100,* 2595–626.

[116] R. Glatz, K. Bailey-Hill, Mimicking nature's noses: From receptor deorphaning to olfactory biosensing, *Prog. Neurobiol.* **2011,** *93,* 270–296.

[117] M. Penza, D. Suriano, G. Cassano, R. Rossi, M. Alvisi, V. Pfister, L. Trizio, M. Brattoli, G. De Gennaro, A gas sensor array for environmental air monitoring: A study case of application of artificial neural networks, *AIP Conf. Proc.* **2011,** *1362,* 205–206.

[118] H.V. Shurmer, An electronic nose: a sensitive and discriminating substitute for a mammalian olfactory system, *IEE Proc. G Circuits, Devices Syst.* **1990,** *137,* 197–204.

[119] A. Perera, T. Sundic, A. Pardo, R. Gutierrez-Osuna, S. Marco, A portable electronic nose based on embedded PC technology and GNU/Linux: Hardware, software and applications, *IEEE Sens. J.* **2002,** *2,* 235–246.

[120] H.T. Chueh, J. V. Hatfield, A real-time data acquisition system for a hand-held electronic nose (H2EN), *Sens. Actuators, B* **2002,** *83,* 262–269.

[121] B.A. Botre, D.C. Gharpure, A.D. Shaligram, Embedded electronic nose and supporting software tool for its parameter optimization, *Sens. Actuators, B* **2010,** *146,* 453–459.

[122] K.T. Tang, S.W. Chiu, C.H. Pan, H.Y. Hsieh, Y.S. Liang, S.C. Liu, Development of a portable electronic nose system for the detection and classification of fruity odors, *Sensors.* **2010,** *10,* 9179–9193.

[123] S. Fuchs, P. Strobel, M. Siadat, M. Lumbreras, Evaluation of unpleasant odor with a portable electronic nose, *Mater. Sci. Eng. C.* **2008,** *28,* 949–953.

[124] L. Zhang, F. Tian, S. Liu, J. Guo, B. Hu, Q. Ye, L. Dang, X. Peng, C. Kadri, J. Feng, Chaos based neural network optimization for concentration estimation of indoor air contaminants by an electronic nose, *Sens. Actuators, A* **2013,** *189,* 161–167.

[125] H.T. Chen, K.T. Ng, A. Bermak, M.K. Law, D. Martinez, Spike latency coding in biologically inspired microelectronic nose, *IEEE Trans. Biomed. Circuits Syst.* **2011,** *5,* 160–168.

[126] S.Y. Park, Y.H. Kim, S.Y. Lee, W. Sohn, J.E. Lee, D.H. Kim, Y.S. Shim, K.C. Kwon, K.S. Choi, H.J. Yoo, J.M. Suh, M. Ko, J.H. Lee, M.J. Lee, S.Y. Kim, M.H. Lee, H.W. Jang, Highly selective and sensitive chemoresistive humidity sensors based on rGO/MoS_2 van der Waals composites, *J. Mater. Chem. A.* **2018,** *6,* 5016–5024.

[127] F.K. Perkins, A.L. Friedman, E. Cobas, P.M. Campbell, G.G. Jernigan, B.T. Jonker, Chemical vapor sensing with monolayer MoS_2, *Nano Lett.* **2013,** *13,* 668–673.

[128] B. Liu, L. Chen, G. Liu, A.N. Abbas, M. Fathi, C. Zhou, High-performance chemical sensing using Schottky-contacted chemical vapor deposition grown monolayer MoS_2 transistors, *ACS Nano.* **2014,** *8,* 5304–5314.

[129] Q. He, Z. Zeng, Z. Yin, H. Li, S. Wu, X. Huang, H. Zhang, Fabrication of flexible MoS_2 thin-film transistor arrays for practical gas-sensing applications, *Small.* **2012,** *8,* 2994–2999.

[130] H. Li, Z. Yin, Q. He, H. Li, X. Huang, G. Lu, D.W.H. Fam, A.I.Y. Tok, Q. Zhang, H. Zhang, Fabrication of single- and multilayer MoS_2 film-based

field-effect transistors for sensing NO at room temperature, *Small.* **2012,** *8,* 63–67.

[131] T.S. Sreeprasad, P. Nguyen, N. Kim, V. Berry, Controlled, defect-guided, metal-nanoparticle incorporation onto MoS_2 via chemical and microwave routes: Electrical, thermal, and structural properties, *Nano Lett.* **2013,** *13,* 4434–4441.

[132] H.C. Choi, M. Shim, S. Bangsaruntip, H. Dai, Spontaneous reduction of metal ions on the sidewalls of carbon nanotubes, *J. Am. Chem. Soc.* **2002,** *124,* 9058–9059.

[133] K.D.B. John F. Moulder, Willian F. Stickle, Peter E. Sobol, 035_Handbook of X-ray Photoelectron Spectroscopy Edited by, (1992).

국문초록

2차원 물질 기반 화학저항식 가스 감지 특성 연구

사물과 연결된 모든 사용자 및 기기와 정보교환을 가능케 하는 사물인터넷 기술의 발달에 따라 기기의 내·외부 정보를 교환하는 스마트센서가 가장 중요한 기술로 고려되고 있다. 특히, 가스 센서는 특정 가스의 존재 및 농도를 검지 할 수 있고 인간의 생활, 안전, 건강, 환경, 에너지 절약에 달하는 수많은 영역에 적용 가능하므로 매우 큰 관심을 불러일으키고 있다. 사물인터넷 혹은 차세대 기기에 적용하려면 가스 센서는 저 소비전력, 저가격, 소형화, 현존 기술과의 접목이 쉬워야 하는 점 등 까다로운 요구사항을 전부 만족시켜야 한다. 오늘날까지 반도체성 금속산화물은 대량생산, 소형화, 저가격, 고온 에서의 높은 가스 반응성 등 여러 장점 덕분에 가스감지물질로 가장 많이 사용되어왔다. 하지만 여전히 낮은 선택성, 고 소비전력, 복잡한 합성 방법 등의 주요 문제점 및 거론된 사물인터넷의 요구사항을 해결하지

못한 채, 대체 가능한 가스 감지물질을 탐색하는 연구가 활발히 진행되고 있다.

대안으로 제시되는 물질 중 대표적으로 그래핀, 전이금속 다이칼코게나이드, 금속산화물 나노시트 같은 2 차원 물질들이 가장 많은 관심을 받고 있다. 2 차원 물질들은 유연성, 높은 비표면적, 많은 활성 사이트, 우수한 상온 가스감지 특성 등 독특하고 우수한 장점들로 인해 금속산화물을 대체하고 미래 기술에 적용 가능하다는 평가를 받는다. 표면 기능화와 귀금속 표면장식을 통해 2 차원 물질 고유 성질의 단점을 개선 및 해결하고, 장점은 극대화할 수 있기 때문에 차세대 가스감지물질로 주목을 받고 있다. 또한 상온 가스감지 특성을 보이며 저가격 대량생산 및 소형화가 쉽고, 기존 기술에 적용하기 쉬운 점 등 실제기기 적용의 요구사항을 만족한다. 하지만 2 차원 물질도 낮은 선택성, 긴 반응시간 및 회복시간, 비가역적 가스감지 특성과 같은 반드시 극복해야 할 약점들을 가지고 있다.

그러므로, 본 논문은 1) 화학적 합성 방법 중 하나인 수열합성 방법과 2) ultra-sonication 을 이용해 물리적으로 합성한 rGO/MoS_2 반데르발스 복합체,

3)귀금속이 표면 장식된 MoS_2, 위의 세가지 샘플로 준비된 화학저항식 가스센서의 감지 특성을 제시하며, 간단한 공정 과정을 통해 저렴한 가격으로 합성을 진행하고, 표면 기능화를 통해 선택성이 낮은 문제 등을 해결했다.

첫 번째로, 간단한 수열합성 방법을 통해 rGO/MoS_2 복합체를 합성하였다. 합성한 물질을 포토리쏘그래피 공정을 통해 제작된 IDE 위에 drop-casting 하여 가스 감지 특성을 확인하였다. rGO/MoS_2 복합체를 기반으로 한 센서는 상온에서 습도에 대해 고 감도, 고 선택성, 가역적 감지 반응을 보였다. 이론적 감지 한계는 약 0.01783% RH 수준으로 계산됐다.

두 번째로, 물리적으로 합성한 rGO/MoS_2 반데르발스 복합체의 습도 감지 특성을 확인하였다. rGO/MoS_2 습도센서는 기타 가스보다 습도에 향상된 반응성, 선택성, 가역성을 보여주었으며, 계산적 상온 감지 한계는 0.0109% RH 정도로 매우 민감했다. 이 센서는 휘어진 형태에서도 안정적인 구동을 보여줄 뿐만 아니라, 장기간이 지난 이후에도 구동이 되는 것이 검증되었다. 이러한 우수한 특성과 손쉬운 제조공정을 이용하여 합성된 rGO/MoS_2

반데르발스 복합체는 사물인터넷 및 웨어러블 전자기기 등 차세대 기술에 실제 적용 잠재성을 넓혔다.

세 번째로, MoS_2의 표면에 용액공정방법을 이용해 귀금속 나노입자를 장식하고 이를 기반으로 한 가스 감지 특성을 분석하였다. 본 실험에서는 Pd, Au, 그리고 Pt를 MoS_2 표면에 합성하였으며, MoS_2의 선택성을 향상시켜 2x2 어레이를 구현하였다. 매우 간단한 제조 공정과 우수한 가스 감지 특성을 기반으로 차세대 가스 감지 물질로써 2차원 MoS_2 잠재성이 높음을 확인할 수 있는 연구이다.

학번: 2015-20816

성명: 박 서연

Keyword: 2 차원 물질, 이황화몰리브덴, 화학저항식 가스센서, 가스센서 어레이, 사물인터넷